

A reduced unified continuum formulation for vascular fluid-structure interaction

Ingrid S. Lan^a, Ju Liu^{b,c,*}, Weiguang Yang^d, Alison L. Marsden^{a,d,e}

^aDepartment of Bioengineering, Stanford University, Stanford, CA 94305, USA

^bDepartment of Mechanics and Aerospace Engineering, Southern University of Science and Technology, Shenzhen, Guangdong 518055, P.R. China

^cGuangdong-Hong Kong-Macao Joint Laboratory for Data-Driven Fluid Mechanics and Engineering Applications, Southern University of Science and Technology, Shenzhen, Guangdong 518055, P.R. China

^dDepartment of Pediatrics (Cardiology), Stanford University, Stanford, CA 94305, USA

^eInstitute for Computational and Mathematical Engineering, Stanford University, Stanford, CA 94305, USA

Abstract

We recently derived the unified continuum and variational multiscale formulation for fluid-structure interaction (FSI) using the Gibbs free energy as the thermodynamic potential. Restricting our attention to vascular FSI, we now reduce this formulation in arbitrary Lagrangian-Eulerian (ALE) coordinates by adopting three common modeling assumptions for the vascular wall. The resulting semi-discrete formulation, referred to as the reduced unified continuum formulation, achieves monolithic coupling of the FSI system in the Eulerian frame through a simple modification of the fluid boundary integral. While ostensibly similar to the semi-discrete formulation of the coupled momentum method introduced by Figueroa et al., its underlying derivation does not rely on an assumption of a fictitious body force in the elastodynamics sub-problem and therefore represents a direct simplification of the ALE method. Furthermore, uniform temporal discretization of the entire FSI system is performed via the generalized- α scheme. In contrast to the predominant approach yielding only first-order accuracy for pressure, we collocate both pressure and velocity at the intermediate time step to achieve uniform second-order temporal accuracy. In conjunction with quadratic tetrahedral elements, our methodology offers higher-order temporal and spatial accuracy for quantities of clinical interest, including pressure and wall shear stress. Furthermore, without loss of consistency, a segregated predictor multi-corrector algorithm is developed to preserve the same block structure as for the incompressible Navier-Stokes equations in the implicit solver's associated linear system. Block preconditioning of a monolithically coupled FSI system is therefore made possible for the first time. Compared to alternative preconditioners, our three-level nested block preconditioner, which achieves improved representation of the Schur complement, demonstrates robust performance over a wide range of physical parameters. We present verification of our methodology against Womersley's deformable wall theory and additionally develop practical modeling techniques for clinical applications, including tissue prestressing. We conclude with an assessment of our combined FSI technology in two patient-specific cases.

Keywords: Fluid-structure interaction, Unified continuum formulation, Variational multiscale method, Nested block preconditioner, Womersley solution, Patient-specific hemodynamics

1. Introduction

Fluid-structure interaction (FSI) problems present the challenge of coupling a deformable structural problem to a fluid problem posed on a domain moving in accordance with the deforming structure. In the last

*Corresponding author

Email addresses: ingridl@stanford.edu (Ingrid S. Lan), liuj36@sustech.edu.cn (Ju Liu), wgyang@stanford.edu (Weiguang Yang), amarsden@stanford.edu (Alison L. Marsden)

four decades, both interface-tracking and interface-capturing methods have been developed to account for the deforming fluid domain. In interface-tracking methods, the coupling interface is resolved by the mesh, and the arbitrary Lagrangian-Eulerian (ALE) formulation is adopted to describe mechanics problems posed on a moving domain [1, 2, 3]; in interface-capturing methods, including the immersed boundary [4, 5] and fictitious domain methods [6], the interface is described implicitly on a background mesh. Whereas applications in cardiac mechanics involving valve leaflet motion largely employ the interface capturing method [7, 8, 9, 10, 11], ventricular and vascular wall deformation are typically modeled with the ALE method [12, 13, 14, 15], allowing for hemodynamic attributes near the wall to be accurately resolved for clinical implications.

In addition to this classification of FSI formulations, FSI coupling strategies can also be categorized into monolithic and partitioned approaches. In monolithic approaches, the coupling conditions, namely the continuity of velocity and stress at the fluid-solid interface, are exactly satisfied [16]. Despite their superior robustness, the resulting system is highly nonlinear [17, 12], requires novel algorithms for the coupled system, and necessitates additional implementation efforts. On the other hand, partitioned methods are generally favored for their modularity, as existing fluid and structure codes can be independently used and loosely coupled via transmission conditions at the fluid-solid interface. Partitioned methods, however, were initially developed for aeroelastic problems [18], in which the structural density is much larger than the fluid density. Numerical instabilities arise in problems involving fluid and structural densities of comparable magnitudes. This so-called added mass effect [19, 20, 21] does not vanish with time step refinement and is particularly pronounced in hydroelastic problems such as cardiovascular FSI problems, where the fluid and structural densities are almost identical. Many approaches, such as generalized Robin-to-Robin transmission conditions [22], have been proposed to improve the stability of partitioned algorithms under the added mass effect. Yet, recent results also suggest that this improved stability may actually be at the expense of critical dynamic characteristics of the structural sub-problem [23], signifying an alarming issue regarding partitioned approaches for hydroelastic problems.

In this work on vascular FSI, we adopt our recently developed unified continuum and variational multi-scale (VMS) formulation [14], a monolithically coupled ALE method. Derived using the Gibbs free energy rather than the Helmholtz free energy as the thermodynamic potential, the formulation bridges the conventionally diverging approaches for computational fluid and solid mechanics. Its ability to naturally recover important continuum models, including viscous fluids and hyperelastic solids, through appropriate constitutive modeling drastically simplifies monolithic FSI coupling. Furthermore, the formulation is well-behaved in both compressible and incompressible regimes, enabling simulation of structural dynamics with a Poisson’s ratio up to 0.5. Given the nontrivial computational expense associated with an ALE formulation, we apply three common modeling assumptions concerning the strain magnitude, geometry, and constitutive model of the vascular wall—the infinitesimal strain, thin-walled, and linear elastic membrane assumptions, respectively—to arrive at our so-called *reduced unified continuum formulation*. The resulting semi-discrete formulation presents a monolithically coupled FSI system posed in an Eulerian frame of reference, in which the structural velocity degrees of freedom are reduced to the fluid velocity degrees of freedom at the fluid-solid interface.

Despite its ostensible similarity to the semi-discrete formulation of the coupled momentum method (CMM), first introduced by Figueroa et al. [24] and recently extended to a nonlinear rotation-free shell formulation [25], the FSI coupling in CMM relies on an assumption of a fictitious body force in the elastodynamics sub-problem, defined in relation to the fluid traction on the wall. While this coupling approach was inspired by Womersley’s derivation of an analytical solution for axisymmetric flow in an elastic pipe [26, 27], we believe this assumption of a fictitious body force is unnecessary. Since its introduction, CMM has been implemented in the open-source blood flow simulation software packages SimVascular [28, 29] and CRIMSON [30] and extensively used in clinical applications ranging from interventions for coronary artery disease [31, 32, 33] and aortic coarctation [34] to single-ventricle physiology [35], and Alagille syndrome [36, 37]. It has also been validated against experimental measurements from compliant in vitro phantom models [38, 39] and Womersley’s analytical solution for axisymmetric flow in a thin, linear elastic pipe subject to an oscillating pressure gradient [40, 41]. While the studies found good agreement for pressure, flow, pulse wave propagation, and wall displacement, Filonova et al. [41] documented large errors in radial velocity.

In this work, stabilized spatial discretization is performed with the residual-based variational multiscale formulation [42], which retains numerical consistency across all scales and exhibits superior performance as a large eddy simulation turbulence model when compared to approaches employing traditional stabilized formulations. We further note that integration-by-parts is not adopted for the divergence operator in the continuity equation for two reasons. First, from an energy perspective, the additional boundary integral term produced from integration-by-parts could pollute the energy dissipation structure in the discrete scheme. In addition, integration-by-parts yields a contradiction in the regularity of the pressure function space in the Galerkin formulation, though this contradiction seems not to produce apparent numerical issues when the stabilized formulation is invoked.

The generalized- α method was initially proposed for structural dynamics as an unconditionally stable and second-order accurate implicit scheme for temporal discretization with user-specified levels of high-frequency dissipation [43]. When Jansen et al. first applied the generalized- α method to the compressible Navier-Stokes equations [44], the pressure primitive variables were uniformly evaluated at the intermediate time step $t_{n+\alpha_f}$. The predominant approach in the computational fluid dynamics (CFD) and FSI communities today [24, 42, 45, 46, 47, 48], however, is to evaluate velocity at the intermediate step but pressure at time step t_{n+1} . While the community continues to reference the second-order temporal accuracy of the generalized- α method, we recently demonstrated that this particular dichotomous approach yields only first-order accuracy in pressure. Concurrent evaluation of velocity and pressure at the intermediate step, as in our approach, recovers second-order accuracy for pressure [49].

In contrast to the use of the Newmark- β method [50] in CMM [24] for temporal integration of membrane displacements, we adopt the fully implicit generalized- α method for uniform temporal discretization of both the fluid and solid sub-problems, enabling second-order accuracy and high-frequency dissipation simultaneously in the full FSI system. With a segregated predictor-multicorrector algorithm we previously used for the unified continuum and VMS formulation [14, 51], the three-by-three block structure for the matrix problem in the consistent Newton-Raphson procedure can be reduced to a two-by-two block structure identical to that of the incompressible Navier-Stokes equations. Not only does this segregated algorithm preserve the consistency of the Newton-Raphson method, but it also enables the use of existing CFD solvers with only minimal modifications. We exploit this preserved two-by-two block structure for preconditioning of the linear system with our three-level nested block preconditioner [51], which attains improved representation of the Schur complement with a “matrix-free” technique to algorithmically define the action of the Schur complement on a vector. Our nested block preconditioning technique is thus robust for cardiovascular simulations involving several contributing terms in the Schur complement of widely varying orders of magnitude, associated with convection, diffusion, vascular wall stiffness, and reduced models at the outlets representing downstream vasculature. We further note that our study represents the first in which block preconditioning is performed for a monolithically coupled FSI system.

The body of this work is organized as follows. In Section 2, the unified continuum and VMS formulation is simplified to our reduced unified continuum formulation for vascular FSI via three modeling assumptions. The spatiotemporal discretization methods and the associated predictor multi-corrector algorithm are also presented. In Section 3, the preconditioning technique for the associated linear system is developed. In Section 4, verification of our reduced unified continuum formulation is performed against the rigid and deformable Womersley benchmark cases using both linear and quadratic tetrahedral elements. Verification of CMM with linear elements is also presented for comparison. In Section 5, we discuss practical modeling techniques for capturing physiological behavior in patient-specific clinical applications. Among these practical modeling techniques is tissue prestressing to account for the nonzero internal stress state of the vascular wall at imaging, which we iteratively update via fixed-point iterations while solving a modified problem over the vascular wall under a fluid traction corresponding to the cardiac phase at imaging. We additionally present a centerline-based approach for variable wall thickness assignment to avoid unphysiological thicknesses produced by previous Laplacian approaches at regions of sharp local changes in geometry. Finally, we conclude with an assessment of our combined FSI technology with two patient-specific cases in Section 6.

2. Governing equations and their spatiotemporal discretization

In this section, we introduce the strong and weak forms of the elastodynamic and incompressible Newtonian fluid problems following the unified continuum formulation [14] and outline the assumptions yielding our reduced unified continuum formulation in the Eulerian description. This monolithically coupled FSI system is then integrated in time using the generalized- α method, which is solved by a segregated predictor multi-corrector algorithm.

2.1. Strong-form problem

We consider a domain $\Omega \subset \mathbb{R}^3$ admitting a non-overlapping subdivision $\overline{\Omega} = \overline{\Omega^f \cup \Omega^s}$, $\emptyset = \Omega^f \cap \Omega^s$, in which Ω^f and Ω^s represent the sub-domains occupied by the fluid and solid materials, respectively. The fluid-solid interface is a two-dimensional manifold denoted by Γ_I , and the boundary $\Gamma := \partial\Omega$ can be partitioned into four non-overlapping subdivisions:

$$\Gamma = \overline{\Gamma_g^f \cup \Gamma_h^f \cup \Gamma_g^s \cup \Gamma_h^s}, \text{ and } \emptyset = \Gamma_g^f \cap \Gamma_h^f = \Gamma_g^f \cap \Gamma_g^s = \Gamma_g^f \cap \Gamma_h^s = \Gamma_h^f \cap \Gamma_h^s = \Gamma_h^f \cap \Gamma_g^s = \Gamma_h^s \cap \Gamma_g^s.$$

In the above, the four subdivisions represent the Dirichlet part of the fluid boundary, the Neumann part of the fluid boundary, the Dirichlet part of the solid boundary, and the Neumann part of the solid boundary, respectively. We note that since the present theory involves multiple unknowns in \mathbb{R}^3 , the boundary Γ should in fact be generalized to admit a different decomposition for each component of each unknown [52, p.77]. To simplify our presentation, however, we consider the same partition of Γ for all unknowns here and note that practical problems would require generalization. We demand Γ to be at least Lipschitz such that the outward normal vector \mathbf{n} is well-defined almost everywhere. We also assume that the interior fluid-solid interface Γ_I is sufficiently smooth such that its outward normal vector is well-defined. In particular, we use \mathbf{n}^f and \mathbf{n}^s to represent the unit outward normal vector on Γ_I relative to Ω^f and Ω^s respectively, such that $\mathbf{n}^f = -\mathbf{n}^s$. Let the time interval of interest be denoted by $(0, T) \subset \mathbb{R}$, with $T > 0$. With this geometric configuration in mind, we state the strong-form sub-problems separately for the two sub-domains.

Under the Stokes' hypothesis and isothermal condition, the initial-boundary value problem in the solid sub-domain Ω^s can be stated as follows in the Lagrangian description [14]. Given the body force per unit mass \mathbf{b}^s , Dirichlet data \mathbf{g}^s , boundary traction \mathbf{h}^s , and initial displacement and velocity fields \mathbf{u}_0^s and \mathbf{v}_0^s , find the solid displacement \mathbf{u}^s , pressure p^s , and velocity \mathbf{v}^s , such that

$$\mathbf{0} = \frac{d\mathbf{u}^s}{dt} - \mathbf{v}^s, \quad \text{in } \Omega^s \times (0, T), \quad (2.1)$$

$$0 = \beta_\theta^s(p^s) \frac{dp^s}{dt} + \nabla \cdot \mathbf{v}^s, \quad \text{in } \Omega^s \times (0, T), \quad (2.2)$$

$$\mathbf{0} = \rho^s(p^s) \frac{d\mathbf{v}^s}{dt} - \nabla \cdot \boldsymbol{\sigma}_{\text{dev}}^s + \nabla p^s - \rho^s(p^s) \mathbf{b}^s, \quad \text{in } \Omega^s \times (0, T), \quad (2.3)$$

$$\mathbf{u}^s = \mathbf{g}^s, \quad \text{on } \Gamma_g^s \times (0, T), \quad (2.4)$$

$$\boldsymbol{\sigma}^s \mathbf{n} = \mathbf{h}^s, \quad \text{on } \Gamma_h^s \times (0, T), \quad (2.5)$$

$$\mathbf{u}^s(\cdot, 0) = \mathbf{u}_0^s(\cdot), \quad \text{in } \bar{\Omega}^s, \quad (2.6)$$

$$\mathbf{v}^s(\cdot, 0) = \mathbf{v}_0^s(\cdot), \quad \text{in } \bar{\Omega}^s. \quad (2.7)$$

Here, β_θ^s is the isothermal compressibility coefficient, ρ^s is the solid density, and $\boldsymbol{\sigma}_{\text{dev}}^s$ is the deviatoric component of the Cauchy stress. To characterize the material behavior, constitutive relations for β_θ^s , ρ^s , and $\boldsymbol{\sigma}_{\text{dev}}^s$ must be provided. Interested readers may refer to [14, Sec. 2.4] for an overview of various constitutive relations for β_θ^s and ρ^s and their relations with different forms of volumetric free energies.

Assumption 1. *The solid deformation is small enough such that the infinitesimal strain theory is valid.*

Under the infinitesimal strain assumption, the reference and current frames coincide, as do the total (d/dt) and partial ($\partial/\partial t$) time derivatives in (2.1)-(2.3). The density $\rho^s(p^s)$ takes the value in the reference

configuration, denoted ρ^s . Furthermore, one may show that $\beta_\theta(p^s) = 1/\kappa^s$, where κ^s is the solid bulk modulus [53, p.941]. Integrating (2.2) in time then yields

$$p^s = -\kappa^s \nabla \cdot \mathbf{u}^s. \quad (2.8)$$

The infinitesimal strain tensor is given by

$$\boldsymbol{\epsilon}(\mathbf{u}^s) := \frac{1}{2} \left(\nabla \mathbf{u}^s + (\nabla \mathbf{u}^s)^T \right) = \boldsymbol{\epsilon}_{\text{dev}}(\mathbf{u}^s) + \frac{1}{3} \nabla \cdot \mathbf{u}^s \mathbf{I},$$

where $\boldsymbol{\epsilon}_{\text{dev}}$ is the strain deviator and \mathbf{I} is the second-order identity tensor. Given a strain energy function $W(\boldsymbol{\epsilon}_{\text{dev}})$, the stress deviator is then

$$\boldsymbol{\sigma}_{\text{dev}}^s = \frac{\partial W(\boldsymbol{\epsilon}_{\text{dev}})}{\partial \boldsymbol{\epsilon}} = \frac{\partial W(\boldsymbol{\epsilon}_{\text{dev}})}{\partial \boldsymbol{\epsilon}_{\text{dev}}} : \frac{\partial \boldsymbol{\epsilon}_{\text{dev}}}{\partial \boldsymbol{\epsilon}} = \mathbb{P}^T \frac{\partial W(\boldsymbol{\epsilon}_{\text{dev}})}{\partial \boldsymbol{\epsilon}_{\text{dev}}}, \quad \mathbb{P} := \mathbb{I} - \frac{1}{3} \mathbf{I} \otimes \mathbf{I},$$

where \mathbb{P} is the deviatoric projector, and \mathbb{I} is the fourth-order symmetric identity tensor. The Cauchy stress for the solid body thus takes the following form,

$$\boldsymbol{\sigma}^s := \boldsymbol{\sigma}_{\text{dev}}^s - p^s \mathbf{I} = \mathbb{P}^T \frac{\partial W(\boldsymbol{\epsilon}_{\text{dev}})}{\partial \boldsymbol{\epsilon}_{\text{dev}}} + \kappa^s \nabla \cdot \mathbf{u}^s \mathbf{I}.$$

Remark 1. *As will be revealed, Assumption 1 renders the eventual FSI formulation implementationally and computationally appealing. While several promising results have been reported in the literature [54, 41], its validity must be judiciously assessed under various physiological settings in both health and disease.*

While the fluid sub-problem in an ALE formulation is indeed posed on a moving domain that tracks the solid deformation, Assumption 1 guarantees this geometry adherence and renders mesh motion unnecessary. The initial-boundary value problem for the incompressible Newtonian fluid in the fluid sub-domain Ω^f can thus be stated as follows. Given the body force per unit mass \mathbf{b}^f , Dirichlet data \mathbf{g}^f , boundary traction \mathbf{h}^f , and divergence-free initial velocity field \mathbf{v}_0^f , find the fluid velocity \mathbf{v}^f and pressure p^f , such that

$$\mathbf{0} = \rho^f \frac{\partial \mathbf{v}^f}{\partial t} + \rho^f \mathbf{v}^f \cdot \nabla \mathbf{v}^f - \nabla \cdot \boldsymbol{\sigma}_{\text{dev}}^f + \nabla p^f - \rho^f \mathbf{b}^f, \quad \text{in } \Omega^f \times (0, T), \quad (2.9)$$

$$0 = \nabla \cdot \mathbf{v}^f, \quad \text{in } \Omega^f \times (0, T), \quad (2.10)$$

$$\mathbf{v}^f = \mathbf{g}^f \quad \text{on } \Gamma_g^f \times (0, T), \quad (2.11)$$

$$\boldsymbol{\sigma}^f \mathbf{n} = \mathbf{h}^f \quad \text{on } \Gamma_h^f \times (0, T), \quad (2.12)$$

$$\mathbf{v}^f(\cdot, 0) = \mathbf{v}_0^f(\cdot), \quad \text{in } \bar{\Omega}^f, \quad (2.13)$$

wherein

$$\boldsymbol{\sigma}_{\text{dev}}^f := 2\mu^f \boldsymbol{\epsilon}_{\text{dev}}(\mathbf{v}^f), \quad \boldsymbol{\epsilon}_{\text{dev}}(\mathbf{v}^f) := \frac{1}{2} \left(\nabla \mathbf{v}^f + (\nabla \mathbf{v}^f)^T \right) - \frac{1}{3} \nabla \cdot \mathbf{v}^f \mathbf{I}. \quad (2.14)$$

Here, ρ^f is the fluid density, $\boldsymbol{\sigma}_{\text{dev}}^f$ is the deviatoric component of the Cauchy stress for a Newtonian fluid, μ^f is the dynamic viscosity, and $\boldsymbol{\epsilon}_{\text{dev}}$ is the deviatoric component of the rate-of-strain tensor.

The strong-form FSI problem can be completed with the following kinematic condition enforcing the continuity of velocity on Γ_I ,

$$\mathbf{v}^f = \mathbf{v}^s, \quad \text{on } \Gamma_I, \quad (2.15)$$

and the following dynamic condition enforcing the continuity of stress,

$$\boldsymbol{\sigma}^f \mathbf{n}^f = -\boldsymbol{\sigma}^s \mathbf{n}^s, \quad \text{on } \Gamma_I. \quad (2.16)$$

Together, Equations (2.1)-(2.16) constitute the coupled strong-form FSI problem, in which the solid problem is restricted to small-strain elastodynamics.

2.2. Semi-discrete formulation

In this section, we present the semi-discrete formulations for the two coupled sub-problems separately. By invoking two more assumptions for the vascular wall, we then reduce the elastodynamics formulation to a thin-walled, linear elastic membrane formulation, yielding a convenient FSI formulation that does not explicitly require solid degrees of freedom. We further note that the reduction to a membrane formulation conveniently bypasses the troublesome procedure of modeling the vascular wall, which current medical imaging techniques largely remain unable to accurately resolve [15].

2.2.1. Semi-discrete formulation for elastodynamics

Let \mathcal{S}_v^s be the trial solution space for the solid velocity; let \mathcal{S}_u^s and \mathcal{V}_u^s denote the trial solution and test function spaces for the solid displacement. We can then state the semi-discrete elastodynamics formulation in Ω^s as follows. Find

$$\mathbf{y}_h^s(t) := \left\{ \mathbf{v}_h^s(t), \mathbf{u}_h^s(t) \right\}^T \in \mathcal{S}_v^s \times \mathcal{S}_u^s$$

such that

$$\begin{aligned} \mathbf{B}_k^s(\dot{\mathbf{y}}_h^s, \mathbf{y}_h^s) &= \mathbf{0}, \\ \mathbf{B}_m^s(\mathbf{w}_h^s; \dot{\mathbf{y}}_h^s, \mathbf{y}_h^s) &= 0, \quad \forall \mathbf{w}_h^s \in \mathcal{V}_u^s, \end{aligned}$$

where

$$\mathbf{B}_k^s(\dot{\mathbf{y}}_h^s, \mathbf{y}_h^s) := \frac{d\mathbf{u}_h^s}{dt} - \mathbf{v}_h^s, \quad (2.17)$$

$$\mathbf{B}_m^s(\mathbf{w}_h^s; \dot{\mathbf{y}}_h^s, \mathbf{y}_h^s) := \int_{\Omega^s} \mathbf{w}_h^s \cdot \rho^s \left(\frac{d\mathbf{v}_h^s}{dt} - \mathbf{b}^s \right) d\Omega + \int_{\Omega^s} \boldsymbol{\epsilon}(\mathbf{w}_h^s) : \boldsymbol{\sigma}^s(\mathbf{u}_h^s) d\Omega - \int_{\Gamma_h^s} \mathbf{w}_h^s \cdot \mathbf{h}^s d\Gamma, \quad (2.18)$$

with $\mathbf{y}_h^s(0) = \{\mathbf{v}_0^s, \mathbf{u}_0^s\}^T$. Here, \mathbf{v}_0^s and \mathbf{u}_0^s are \mathcal{L}^2 projections of the initial velocity and displacement fields onto the discrete spaces \mathcal{S}_v^s and \mathcal{S}_u^s , respectively.

Remark 2. In contrast to the conventional “acceleration form” in which only displacement degrees-of-freedom are utilized, acceleration is represented here as the first time derivative of velocity via the kinematic relation (2.17) [55]. While this “momentum form” ostensibly introduces three additional velocity degrees of freedom on each node in Ω^s , we will later show that (2.17) does not enter the implicit solution procedure for the fully discrete formulation. Furthermore, as will be discussed later, this first-order structural dynamics formulation is favorable for temporal discretization via the generalized- α method.

Restricting our discussion to vascular FSI, we now introduce our second assumption pertaining to the vascular wall geometry.

Assumption 2. Ω^s is thin in one direction and can thus be parameterized by the fluid-solid interface Γ_I and a through-thickness coordinate in the unit outward normal direction.

To simplify our presentation, let Γ_I be parameterized by a single chart $\Xi \subset \mathbb{R}^2$, a bounded open set. Let $\boldsymbol{\chi}(\xi, \eta)$ be a smooth one-to-one mapping of $(\xi, \eta) \in \Xi$ onto the fluid-solid interface $\boldsymbol{\chi} \in \Gamma_I$, where $\boldsymbol{\chi}$ represents the position vector of a generic point on Γ_I . The unit outward normal vector to Ω^f can be represented by

$$\mathbf{n}^f = \frac{\mathbf{e}_\xi \times \mathbf{e}_\eta}{\|\mathbf{e}_\xi \times \mathbf{e}_\eta\|}, \quad \text{where} \quad \mathbf{e}_\xi := \frac{\partial \boldsymbol{\chi}}{\partial \xi} / \left\| \frac{\partial \boldsymbol{\chi}}{\partial \xi} \right\|, \quad \mathbf{e}_\eta := \frac{\partial \boldsymbol{\chi}}{\partial \eta} / \left\| \frac{\partial \boldsymbol{\chi}}{\partial \eta} \right\|.$$

Given this thin-walled assumption, we can introduce the following diffeomorphism from $\boldsymbol{\xi} := \{\xi, \eta, \zeta\} \in \Xi \times (0, 1)$ to $\mathbf{x} \in \Omega^s$,

$$\mathbf{x}(\boldsymbol{\xi}) = \mathbf{x}(\xi, \eta, \zeta) := \boldsymbol{\chi}(\xi, \eta) + \zeta \mathbf{h}^s(\xi, \eta) \mathbf{n}^f, \quad (2.19)$$

where ξ and η are the in-plane parametric coordinates, h^s is the wall thickness as a function of ξ and η , and $\zeta \in (0, 1)$ is the through-thickness parametric coordinate. For any fixed ζ , the surface defined by this parameterization of Ω^s is a lamina, and a corresponding lamina coordinate system $\{\mathbf{e}_1^l, \mathbf{e}_2^l, \mathbf{e}_3^l\}$, denoted with a superscript l , may be constructed as follows [52, Sec. 6.2],

$$\mathbf{e}_1^l := \frac{\sqrt{2}}{2}(\mathbf{e}_\alpha - \mathbf{e}_\beta), \quad \mathbf{e}_2^l := \frac{\sqrt{2}}{2}(\mathbf{e}_\alpha + \mathbf{e}_\beta), \quad \mathbf{e}_3^l := \mathbf{n}^f,$$

in which,

$$\mathbf{e}_\alpha := \frac{1}{2}(\mathbf{e}_\xi + \mathbf{e}_\eta) / \left\| \frac{1}{2}(\mathbf{e}_\xi + \mathbf{e}_\eta) \right\|, \quad \mathbf{e}_\beta := \mathbf{e}_3^l \times \mathbf{e}_\alpha / \|\mathbf{e}_3^l \times \mathbf{e}_\alpha\|.$$

With these lamina basis vectors $\{\mathbf{e}_i^l\}_{i=1}^3$, the coordinate transformation from the global coordinates \mathbf{x} to the local lamina coordinates \mathbf{x}^l is then given by $\mathbf{x}^l = \mathbf{Q}\mathbf{x}$ with the rotation matrix

$$\mathbf{Q} := [\mathbf{e}_1^l \quad \mathbf{e}_2^l \quad \mathbf{e}_3^l]^T.$$

From the parameterization (2.19), we have

$$\begin{aligned} j := \det \left(\frac{\partial \mathbf{x}}{\partial \boldsymbol{\xi}} \right) &= h^s \mathbf{n}^f \cdot \left(\frac{\partial \mathbf{x}}{\partial \xi} \times \frac{\partial \mathbf{x}}{\partial \eta} \right) = h^s \mathbf{n}^f \cdot \left(\left(\frac{\partial \boldsymbol{\chi}}{\partial \xi} + \zeta \frac{\partial h^s}{\partial \xi} \mathbf{n}^f \right) \times \left(\frac{\partial \boldsymbol{\chi}}{\partial \eta} + \zeta \frac{\partial h^s}{\partial \eta} \mathbf{n}^f \right) \right) \\ &= h^s \mathbf{n}^f \cdot \left(\frac{\partial \boldsymbol{\chi}}{\partial \xi} \times \frac{\partial \boldsymbol{\chi}}{\partial \eta} \right), \end{aligned}$$

indicating the following transformation of the volume element from $\Xi \times (0, 1)$ to Ω^s ,

$$d\Omega^s := d\mathbf{x} = j d\boldsymbol{\xi} = j d\xi d\eta d\zeta = h^s \mathbf{n}^f \cdot \left(\frac{\partial \boldsymbol{\chi}}{\partial \xi} \times \frac{\partial \boldsymbol{\chi}}{\partial \eta} \right) d\xi d\eta d\zeta = h^s \mathbf{n}^f \cdot \mathbf{n}^f d\Gamma_I d\zeta = h^s d\Gamma_I d\zeta, \quad (2.20)$$

where we have utilized the transformation of the area element from Ξ to Γ_I ,

$$\mathbf{n}^f d\Gamma_I = \left(\frac{\partial \boldsymbol{\chi}}{\partial \xi} \times \frac{\partial \boldsymbol{\chi}}{\partial \eta} \right) d\xi d\eta.$$

The volume integral over Ω^s can thus be simplified in the following manner,

$$\int_{\Omega^s} (\cdot) d\Omega = \int_{\Gamma_I} h^s \int_0^1 (\cdot) d\zeta d\Gamma. \quad (2.21)$$

We finally introduce the following membrane assumption for the vascular wall.

Assumption 3. *The displacement \mathbf{u}^s is a function of the in-plane parametric coordinates (ξ, η) only, and the transverse normal stress $\boldsymbol{\sigma}_{33}^s$ is zero in the \mathbf{e}_3^l direction of the lamina system.*

Cardiac pulse wavelengths are at least three orders of magnitude larger than arterial diameters [56], causing vessels to respond to transverse loading primarily with in-plane stresses rather than bending stresses. Out-of-plane rotations and their corresponding bending effects are thus neglected under this membrane assumption, minimizing the number of degrees of freedom and facilitating convenient fluid-solid coupling. In addition, to avoid thickness locking, also known as Poisson thickness locking in classical shell theories, the transverse normal stress is assumed to vanish, which has been well-substantiated over time [57, 58]. Furthermore, it is commonly known that when the linear, constant strain triangle is used to model membrane components experiencing transverse loads in three-dimensional structures, it suffers from severe transverse and in-plane shear locking, thereby demonstrating overly stiff behavior [59, 60]. Transverse shear modes are therefore added to stabilize the linear membrane.

We now define the solid constitutive relation in the lamina coordinate system to enforce the zero transverse normal stress condition. Considering the strain energy for isotropic linear elasticity,

$$W(\boldsymbol{\epsilon}_{\text{dev}}) = \mu \boldsymbol{\epsilon}_{\text{dev}} : \boldsymbol{\epsilon}_{\text{dev}},$$

the constitutive relation is given by

$$\boldsymbol{\sigma}_{\text{dev}}^{s,l} = 2\mu^s \boldsymbol{\epsilon}_{\text{dev}}(\mathbf{u}^{s,l}).$$

Recalling from (2.8) that the hydrostatic component of the Cauchy stress is already given by $p^s = -\kappa^s \nabla \cdot \mathbf{u}^{s,l}$, the Cauchy stress can be written as

$$\boldsymbol{\sigma}^{s,l} = \boldsymbol{\sigma}_{\text{dev}}^{s,l} - p^s \mathbf{I} = \mathbb{C}^{s,l} \boldsymbol{\epsilon}^l(\mathbf{u}^{s,l}), \quad \text{with} \quad \mathbb{C}^{s,l} := 2\mu^s(\mathbf{x}^l) \mathbb{I} + \lambda^s(\mathbf{x}^l) \mathbf{I} \otimes \mathbf{I},$$

wherein

$$\begin{aligned} \boldsymbol{\sigma}^{s,l} &= \left\{ \sigma_I^{s,l} \right\} = \left[\sigma_{11}^{s,l}, \sigma_{22}^{s,l}, \sigma_{12}^{s,l}, \sigma_{23}^{s,l}, \sigma_{31}^{s,l} \right]^T, \\ \boldsymbol{\epsilon}^l(\mathbf{u}^{s,l}) &= \left\{ \epsilon_I^l \right\} = \left[\epsilon_{11}^l, \epsilon_{22}^l, 2\epsilon_{12}^l, 2\epsilon_{23}^l, 2\epsilon_{31}^l \right]^T = \left[u_{1,1}^{s,l}, u_{2,2}^{s,l}, u_{1,2}^{s,l} + u_{2,1}^{s,l}, u_{3,2}^{s,l}, u_{3,1}^{s,l} \right]^T, \\ \mathbb{C}^{s,l} &= \left[\mathbb{C}_{IJ}^{s,l} \right] = \frac{E}{(1-\nu^2)} \begin{bmatrix} 1 & \nu & & & \\ \nu & 1 & & & \\ & & \frac{1-\nu}{2} & & \\ & & & \kappa \frac{(1-\nu)}{2} & \\ & & & & \kappa \frac{(1-\nu)}{2} \end{bmatrix} \end{aligned}$$

in Voigt notation. Here, μ^s and λ^s are the Lamé parameters related to the bulk modulus κ^s through the relation $\kappa^s := 2\mu^s/3 + \lambda^s$, E is the Young's modulus, ν is the Poisson's ratio, and $\kappa = 5/6$ is the shear correction factor [52, p.391]. Now adopting the full tensor notation rather than Voigt notation, the Cauchy stress in the lamina coordinate system can be rotated to the global coordinate system by

$$\boldsymbol{\sigma}^s = \mathbf{Q}^T \boldsymbol{\sigma}^{s,l} \mathbf{Q}.$$

Assumption 3 further enables evaluation of (\cdot) in (2.21) at $\zeta = 0$, thereby reducing the volume integral over Ω^s to a surface integral over Γ_I ,

$$\int_{\Omega^s} (\cdot) d\Omega \approx \int_{\Gamma_I} h^s(\cdot) |_{\zeta=0} d\Gamma. \quad (2.22)$$

Remark 3. *The choice of a linear constitutive model can be well justified by experimental canine aortic and pulmonary arterial data exhibiting linearity within the physiological range of pressures [61, 62]. Nonetheless, material nonlinearity and anisotropy could instead be considered using an alternative form for the strain energy function $W(\boldsymbol{\epsilon}_{\text{dev}})$ in the above derivation. We note that for problems characterized by large deformation, such as hypertensive clinical cases, Assumptions 2 and 3 could still be invoked, yet an ALE description of the fluid sub-problem would be required, necessitating mesh motion and rendering the overall FSI formulation less computationally appealing.*

2.2.2. Residual-based VMS formulation for an incompressible Newtonian fluid

Let \mathcal{S}_v^f and \mathcal{S}_p^f denote the trial solution spaces for the fluid velocity and pressure, and let \mathcal{V}_v^f and \mathcal{V}_p^f be their corresponding test function spaces. We can then construct the semi-discrete fluid formulation in Ω^f using the residual-based VMS formulation [42] as follows. Find

$$\mathbf{y}_h^f(t) := \left\{ \mathbf{v}_h^f(t), p_h^f(t) \right\}^T \in \mathcal{S}_v^f \times \mathcal{S}_p^f$$

such that

$$\mathbf{B}_m^f(\mathbf{w}_h^f; \dot{\mathbf{y}}_h^f, \mathbf{y}_h^f) = 0, \quad \forall \mathbf{w}_h^f \in \mathcal{V}_v^f, \quad (2.23)$$

$$\mathbf{B}_c^f(q_h^f; \dot{\mathbf{y}}_h^f, \mathbf{y}_h^f) = 0, \quad \forall q_h^f \in \mathcal{V}_p^f, \quad (2.24)$$

where

$$\mathbf{B}_m^f(\mathbf{w}_h^f; \dot{\mathbf{y}}_h^f, \mathbf{y}_h^f) := \mathbf{B}_m^{\text{vol}}(\mathbf{w}_h^f; \dot{\mathbf{y}}_h^f, \mathbf{y}_h^f) + \mathbf{B}_m^h(\mathbf{w}_h^f; \dot{\mathbf{y}}_h^f, \mathbf{y}_h^f) + \mathbf{B}_m^{\text{bf}}(\mathbf{w}_h^f; \dot{\mathbf{y}}_h^f, \mathbf{y}_h^f), \quad (2.25)$$

$$\begin{aligned} \mathbf{B}_m^{\text{vol}}(\mathbf{w}_h^f; \dot{\mathbf{y}}_h^f, \mathbf{y}_h^f) &:= \int_{\Omega^f} \mathbf{w}_h^f \cdot \rho^f \left(\frac{\partial \mathbf{v}_h^f}{\partial t} + \mathbf{v}_h^f \cdot \nabla \mathbf{v}_h^f - \mathbf{b}^f \right) d\Omega - \int_{\Omega^f} \nabla \cdot \mathbf{w}_h^f p_h^f d\Omega + \int_{\Omega^f} 2\mu^f \boldsymbol{\varepsilon}(\mathbf{w}_h^f) : \boldsymbol{\varepsilon}(\mathbf{v}_h^f) d\Omega \\ &\quad - \int_{\Omega^{f'}} \nabla \mathbf{w}_h^f : (\rho^f \mathbf{v}' \otimes \mathbf{v}_h^f) d\Omega + \int_{\Omega^{f'}} \nabla \mathbf{v}_h^f : (\rho^f \mathbf{w}_h^f \otimes \mathbf{v}') d\Omega - \int_{\Omega^{f'}} \nabla \mathbf{w}_h^f : (\rho^f \mathbf{v}' \otimes \mathbf{v}') d\Omega \\ &\quad - \int_{\Omega^{f'}} \nabla \cdot \mathbf{w}_h^f p' d\Omega, \end{aligned} \quad (2.26)$$

$$\mathbf{B}_m^h(\mathbf{w}_h^f; \dot{\mathbf{y}}_h^f, \mathbf{y}_h^f) := - \int_{\Gamma_h^f} \mathbf{w}_h^f \cdot \mathbf{h}^f d\Gamma, \quad (2.27)$$

$$\mathbf{B}_m^{\text{bf}}(\mathbf{w}_h^f; \dot{\mathbf{y}}_h^f, \mathbf{y}_h^f) := - \int_{\Gamma_h^f} \rho^f \beta(\mathbf{v}_h^f \cdot \mathbf{n}^f)_- \mathbf{w}_h^f \cdot \mathbf{v}_h^f d\Gamma, \quad (2.28)$$

$$\mathbf{B}_c^f(q_h^f; \dot{\mathbf{y}}_h^f, \mathbf{y}_h^f) := \int_{\Omega^f} q_h^f \nabla \cdot \mathbf{v}_h^f d\Omega - \int_{\Omega^{f'}} \nabla q_h^f \cdot \mathbf{v}' d\Omega, \quad (2.29)$$

$$\mathbf{v}' := -\tau_M \left(\rho^f \frac{\partial \mathbf{v}_h^f}{\partial t} + \rho^f \mathbf{v}_h^f \cdot \nabla \mathbf{v}_h^f + \nabla p_h^f - \mu^f \Delta \mathbf{v}_h^f - \rho^f \mathbf{b}^f \right), \quad (2.30)$$

$$p' := -\tau_C \nabla \cdot \mathbf{v}_h^f, \quad (2.31)$$

$$\tau_M := \frac{1}{\rho^f} \left(\frac{C_T}{\Delta t^2} + \mathbf{v}_h^f \cdot \mathbf{G} \mathbf{v}_h^f + C_I \left(\frac{\mu^f}{\rho^f} \right)^2 \mathbf{G} : \mathbf{G} \right)^{-\frac{1}{2}}, \quad (2.32)$$

$$\tau_C := \frac{1}{\tau_M \text{tr} \mathbf{G}}, \quad (2.33)$$

$$G_{ij} := \sum_{k=1}^3 \frac{\partial y_k}{\partial x_i} M_{kl} \frac{\partial y_l}{\partial x_j}, \quad (2.34)$$

$$\mathbf{M} = [M_{kl}] = \frac{\sqrt[3]{2}}{2} \begin{bmatrix} 2 & 1 & 1 \\ 1 & 2 & 1 \\ 1 & 1 & 2 \end{bmatrix}, \quad (2.35)$$

$$\mathbf{G} : \mathbf{G} := \sum_{i,j=1}^3 G_{ij} G_{ij}, \quad (2.36)$$

$$\text{tr} \mathbf{G} := \sum_{i=1}^3 G_{ii}, \quad (2.37)$$

$$(\mathbf{v}_h^f \cdot \mathbf{n}^f)_- := \frac{\mathbf{v}_h^f \cdot \mathbf{n}^f - |\mathbf{v}_h^f \cdot \mathbf{n}^f|}{2} = \begin{cases} \mathbf{v}_h^f \cdot \mathbf{n}^f & \text{if } \mathbf{v}_h^f \cdot \mathbf{n}^f < 0, \\ 0 & \text{if } \mathbf{v}_h^f \cdot \mathbf{n}^f \geq 0. \end{cases} \quad (2.38)$$

Here, $\mathbf{y} = \{y_i\}_{i=1}^3$ are natural coordinates in the parent domain; C_I depends on the polynomial order of the finite element basis functions, taking the values of 36 and 60 for linear and quadratic interpolations, respectively [24, 63]; and C_T is taken to be 4 [14, 51]. \mathbf{B}_m^{bf} is an additional convective traction shown to be robust in overcoming backflow divergence [64, 65], a well-known issue in cardiovascular simulations. It can

be shown that taking $\beta = 1.0$ guarantees energy stability for the numerical scheme adopted here. In this work, β is fixed to be 0.2 to minimize its impact on the flow field and to improve robustness at larger time steps.

Remark 4. *In contrast to CMM [40, 24, 66], integration-by-parts is not performed for the divergence operator in the continuity equation, which could otherwise lead to a loss of energy stability in the Galerkin formulation. Interested readers may refer to [67] for a thorough discussion of the Galerkin formulation for the Navier-Stokes equations. In addition, we adopt the residual-based variational multiscale formulation [42], which has been shown to capture the correct energy spectrum and decay of kinetic energy in isotropic and wall-bounded turbulent flows [42, 68, 69]. The conventional streamline upwind Petrov-Galerkin/pressure-stabilizing Petrov-Galerkin (SUPG/PSPG) method [70, 63], on the other hand, cannot correctly describe the energy spectrum and is thus physically inappropriate as a subgrid-scale model [71]. Furthermore, the stabilization parameters are defined to be invariant to cyclic permutations of node numbering [72, 73].*

2.2.3. Reduced unified continuum formulation for vascular FSI

Discretization of the entire domain Ω by a single mesh with continuous basis functions across the fluid-solid interface Γ_I immediately guarantees satisfaction of the kinematic coupling condition (2.15) in the semi-discrete formulation. The implied relation

$$\mathbf{w}_h^f = \mathbf{w}_h^s, \quad \text{on } \Gamma_I \quad (2.39)$$

also yields weak satisfaction of the traction coupling condition (2.16), that is

$$0 = \int_{\Gamma_I} \mathbf{w}_h^f \cdot (\boldsymbol{\sigma}^f \mathbf{n}^f + \boldsymbol{\sigma}^s \mathbf{n}^s) d\Gamma = \int_{\Gamma_I} \mathbf{w}_h^f \cdot (\boldsymbol{\sigma}^f \mathbf{n}^f - \boldsymbol{\sigma}^s \mathbf{n}^f) d\Gamma.$$

With this mesh choice, the momentum balances (2.18) and (2.25) over Ω^s and Ω^f , respectively, can then be combined into a single momentum balance over the entire continuum body Ω ,

$$\mathbf{B}_m^s(\mathbf{w}_h^s; \dot{\mathbf{y}}_h^s, \mathbf{y}_h^s) + \mathbf{B}_m^f(\mathbf{w}_h^f; \dot{\mathbf{y}}_h^f, \mathbf{y}_h^f) = 0, \quad \forall \mathbf{w}_h^s \in \mathcal{V}_u^s \quad \text{and} \quad \forall \mathbf{w}_h^f \in \mathcal{V}_v^f.$$

Having applied the outlined assumptions to collapse the three-dimensional elastodynamic problem in Ω^s to a two-dimensional problem posed on Γ_I , we now present the reduced semi-discrete FSI formulation. Let \mathbf{u}_h^w be the membrane displacement on Γ_I . Using the kinematic coupling condition (2.15), continuity of test functions on Γ_I (2.39), and the transformation of volume integrals over Ω^s (2.22), we can rewrite the kinematic equation (2.17) as

$$\mathbf{B}_k(\dot{\mathbf{y}}_h, \mathbf{y}_h) := \frac{d\mathbf{u}_h^w}{dt} - \mathbf{v}_h^f = \mathbf{0}, \quad \text{on } \Gamma_I, \quad (2.40)$$

and the momentum balance (2.18) over Ω^s as

$$\mathbf{B}_m^w(\mathbf{w}_h^f; \dot{\mathbf{y}}_h, \mathbf{y}_h) := \int_{\Gamma_I} \mathbf{w}_h^f \cdot \rho^s h^s \left(\frac{d\mathbf{v}_h^f}{dt} - \mathbf{b}^s \right) d\Gamma + \int_{\Gamma_I} h^s \boldsymbol{\epsilon}(\mathbf{w}_h^f) : \boldsymbol{\sigma}^s(\mathbf{u}_h^w) d\Gamma - \int_{\partial\Gamma_I \cap \Gamma_s^h} h^s \mathbf{w}_h^f \cdot \mathbf{h}^s d\Gamma, \quad (2.41)$$

where $\partial\Gamma_I \cap \Gamma_s^h$ constitutes the Neumann partition of the boundary of Γ_I . Finally, let \mathcal{S}_u^w be the trial solution space for \mathbf{u}_h^w . Our reduced unified continuum formulation posed only in the fluid domain Ω_f is then stated as follows. Find

$$\mathbf{y}_h(t) := \left\{ \mathbf{u}_h^w(t), \mathbf{v}_h^f(t), p_h^f(t) \right\}^T \in \mathcal{S}_u^w \times \mathcal{S}_v^f \times \mathcal{S}_p^f$$

such that

$$\mathbf{B}_k(\dot{\mathbf{y}}_h, \mathbf{y}_h) = \mathbf{0}, \quad (2.42)$$

$$\mathbf{B}_m(\mathbf{w}_h^f; \dot{\mathbf{y}}_h, \mathbf{y}_h) := \mathbf{B}_m^w(\mathbf{w}_h^f; \dot{\mathbf{y}}_h, \mathbf{y}_h) + \mathbf{B}_m^f(\mathbf{w}_h^f; \dot{\mathbf{y}}_h^f, \mathbf{y}_h^f) = 0, \quad \forall \mathbf{w}_h^f \in \mathcal{V}_v^f, \quad (2.43)$$

$$\mathbf{B}_c(q_h^f; \dot{\mathbf{y}}_h, \mathbf{y}_h) := \mathbf{B}_c^f(q_h^f; \dot{\mathbf{y}}_h^f, \mathbf{y}_h^f) = 0, \quad \forall q_h^f \in \mathcal{V}_p^f. \quad (2.44)$$

It is then clear that compared to the fluid sub-problem, the above FSI formulation (2.42)-(2.44) consists of an additional coupling relation (2.42) and four additional terms corresponding to the vascular wall's mass, body force, stiffness, and boundary traction, all of which are embedded in (2.43) through the form \mathbf{B}_m^w . Importantly, (2.43) represents the semi-discrete formulation for momentum balance over the entire continuum body consisting of both the fluid and vascular wall. This FSI formulation therefore offers a computationally efficient approach for capturing vascular wall deformation on a stationary fluid mesh.

Remark 5. *Despite the ostensible similarity between our reduced unified continuum formulation and the semi-discrete formulation of CMM, the fluid-solid coupling in CMM was achieved via a fictitious body force assumed to be uniformly distributed through the vessel thickness [24, 40] (see also [74, p.10] and [75, p.119]). Our recent development of the unified continuum and VMS formulation renders this assumption unnecessary for achieving the desired coupling. Starting from the unified formulation in ALE coordinates, we have instead arrived at a similar reduced FSI formulation simply by invoking the small-strain, thin-walled, and membrane assumptions for the solid sub-problem. We further note that the wall thickness has not been assumed to be uniform over each element and thus appears within the integrals over Γ_I in our formulation.*

2.3. Fully discrete formulation

To arrive at the fully discrete FSI formulation, we apply the generalized- α method for temporal discretization of the first-order dynamic system. Let the time interval of interest $(0, T)$ be divided into N_{ts} subintervals of equal size $\Delta t_n := t_{n+1} - t_n$ and delimited by a discrete time vector $\{t_n\}_{n=0}^{N_{ts}}$. The approximations of the solution vector and its time-derivative at time step t_n are denoted as

$$\mathbf{y}_n := \{\mathbf{u}_n^w, \mathbf{v}_n^f, p_n^f\}, \quad \text{and} \quad \dot{\mathbf{y}}_n := \{\dot{\mathbf{u}}_n^w, \dot{\mathbf{v}}_n^f, \dot{p}_n^f\}.$$

Let N_A represent basis functions for all variational spaces, and let $\{\mathbf{e}_i\}$ be the Cartesian basis vectors with $i = 1, 2, 3$. We may then define the residual vectors as follows,

$$\begin{aligned} \mathbf{R}_k(\dot{\mathbf{y}}_n, \mathbf{y}_n) &:= \{\mathbf{B}_k(\dot{\mathbf{y}}_n, \mathbf{y}_n)\}, \\ \mathbf{R}_m(\dot{\mathbf{y}}_n, \mathbf{y}_n) &:= \{\mathbf{B}_m(N_A \mathbf{e}_i; \dot{\mathbf{y}}_n, \mathbf{y}_n)\}, \\ \mathbf{R}_c(\dot{\mathbf{y}}_n, \mathbf{y}_n) &:= \{\mathbf{B}_c(N_A; \dot{\mathbf{y}}_n, \mathbf{y}_n)\}. \end{aligned}$$

The fully discrete scheme can be stated as follows. At time step t_n , given $\dot{\mathbf{y}}_n, \mathbf{y}_n$, and the time step size Δt_n , find $\dot{\mathbf{y}}_{n+1}$ and \mathbf{y}_{n+1} such that

$$\mathbf{R}_k(\dot{\mathbf{y}}_{n+\alpha_m}, \mathbf{y}_{n+\alpha_f}) = \mathbf{0}, \quad (2.45)$$

$$\mathbf{R}_m(\dot{\mathbf{y}}_{n+\alpha_m}, \mathbf{y}_{n+\alpha_f}) = \mathbf{0}, \quad (2.46)$$

$$\mathbf{R}_c(\dot{\mathbf{y}}_{n+\alpha_m}, \mathbf{y}_{n+\alpha_f}) = \mathbf{0}, \quad (2.47)$$

$$\dot{\mathbf{y}}_{n+\alpha_m} = \dot{\mathbf{y}}_n + \alpha_m (\dot{\mathbf{y}}_{n+1} - \dot{\mathbf{y}}_n), \quad (2.48)$$

$$\mathbf{y}_{n+\alpha_f} = \mathbf{y}_n + \alpha_f (\mathbf{y}_{n+1} - \mathbf{y}_n), \quad (2.49)$$

$$\mathbf{y}_{n+1} = \mathbf{y}_n + \Delta t_n \dot{\mathbf{y}}_n + \gamma \Delta t_n (\dot{\mathbf{y}}_{n+1} - \dot{\mathbf{y}}_n). \quad (2.50)$$

In the above system, the three parameters α_m , α_f , and γ determine critical numerical properties of the discrete dynamic system. For linear problems, the following parameterization has been shown to achieve second-order accuracy, unconditional stability, and optimal high frequency dissipation,

$$\alpha_m = \frac{1}{2} \left(\frac{3 - \varrho_\infty}{1 + \varrho_\infty} \right), \quad \alpha_f = \frac{1}{1 + \varrho_\infty}, \quad \gamma = \frac{1}{2} + \alpha_m - \alpha_f,$$

wherein $\varrho_\infty \in [0, 1]$ is the spectral radius of the amplification matrix at the highest mode [44, 43]. In this work, we choose $\varrho_\infty = 0.5$.

Remark 6. While the Newmark- β method [50] used to integrate membrane dynamics in CMM [24] has classically been used in structural dynamics and persists in today's solvers, it faces several well-documented issues. First, it cannot simultaneously achieve second-order accuracy and high-frequency algorithmic damping; second, all first-order implementations of the Newmark- β method are overly dissipative in the mid-frequency modes [52, p.501]; third, implicit schemes of the Newmark family are “not designed to conserve energy and also fail to conserve momentum” for nonlinear structural dynamics [76]. As a result, despite its pervasiveness, the Newmark- β method is not recommended for structural dynamics [77, 55].

Remark 7. The generalized- α method was initially proposed as an integration scheme for structural dynamics [43] and has since been applied to fluid dynamics [44] as well as FSI problems [45]. It exhibits all of the desirable attributes of a competitive integration scheme for structural dynamics, as noted by Hilber and Hughes [77]. Moreover, when applied to a first-order structural dynamic system, it was recently found not to suffer from the ‘overshoot’ phenomenon, a long-standing issue in computational structural dynamics, and to further possess smaller dissipation and dispersion errors than when applied to a second-order system [78]. The generalized- α method is thus highly recommended for integrating inertial type problems.

Remark 8. In both CFD and FSI literature, the fluid velocity and pressure are typically treated dichotomously in the generalized- α method for the incompressible Navier-Stokes equations, such that pressure is collocated at time step t_{n+1} rather than the intermediate time step $t_{n+\alpha_f}$ [24, 68, 66, 79]. Despite the commonly cited second-order accuracy of the generalized- α method, we recently demonstrated that this particular approach yields only first-order temporal accuracy, at least, for pressure. Evaluating pressure at $t_{n+\alpha_f}$ recovers second-order accuracy for the overall algorithm, simplifies the implementation, and resolves a troubling issue in geometric multiscale modeling. Interested readers are referred to [49] for details.

2.4. A segregated predictor multi-corrector algorithm

The fully discrete scheme can be solved iteratively with a predictor multi-corrector algorithm, in which the Newton-Raphson method is used in the multi-corrector iterations to improve the initial prediction. Let $\mathbf{y}_{n+1,(l)}$ and $\dot{\mathbf{y}}_{n+1,(l)}$ denote the solution vector and its time derivative at time step t_{n+1} at the l -th Newton-Raphson iteration, where $n = 0, 1, \dots, N_{ts} - 1$ and $l = 0, 1, \dots, l_{\max}$,

$$\mathbf{y}_{n+1,(l)} := \{\mathbf{u}_{n+1,(l)}^w, \mathbf{v}_{n+1,(l)}^f, p_{n+1,(l)}^f\}, \quad \text{and} \quad \dot{\mathbf{y}}_{n+1,(l)} := \{\dot{\mathbf{u}}_{n+1,(l)}^w, \dot{\mathbf{v}}_{n+1,(l)}^f, \dot{p}_{n+1,(l)}^f\}.$$

We can then denote the residual vectors at iteration number l as

$$\begin{aligned} \mathbf{R}_{(l)} &:= \{\mathbf{R}_{k,(l)}, \mathbf{R}_{m,(l)}, \mathbf{R}_{c,(l)}\}^T, \\ \mathbf{R}_{k,(l)} &:= \mathbf{R}_k(\dot{\mathbf{y}}_{n+\alpha_m,(l)}, \mathbf{y}_{n+\alpha_f,(l)}), \\ \mathbf{R}_{m,(l)} &:= \mathbf{R}_m(\dot{\mathbf{y}}_{n+\alpha_m,(l)}, \mathbf{y}_{n+\alpha_f,(l)}), \\ \mathbf{R}_{c,(l)} &:= \mathbf{R}_c(\dot{\mathbf{y}}_{n+\alpha_m,(l)}, \mathbf{y}_{n+\alpha_f,(l)}), \end{aligned}$$

and the consistent tangent matrix as

$$\mathbf{K}_{(l)} = \begin{bmatrix} \mathbf{K}_{k,(l),\dot{\mathbf{u}}^w} & \mathbf{K}_{k,(l),\dot{\mathbf{v}}^f} & \mathbf{K}_{k,(l),\dot{p}^f} \\ \mathbf{K}_{m,(l),\dot{\mathbf{u}}^w} & \mathbf{K}_{m,(l),\dot{\mathbf{v}}^f} & \mathbf{K}_{m,(l),\dot{p}^f} \\ \mathbf{K}_{c,(l),\dot{\mathbf{u}}^w} & \mathbf{K}_{c,(l),\dot{\mathbf{v}}^f} & \mathbf{K}_{c,(l),\dot{p}^f} \end{bmatrix},$$

wherein

$$\begin{aligned}
\mathbf{K}_{k,(l),\dot{\mathbf{u}}^w} &:= \alpha_m \frac{\partial \mathbf{R}_k(\dot{\mathbf{y}}_{n+\alpha_m,(l)}, \mathbf{y}_{n+\alpha_f,(l)})}{\partial \dot{\mathbf{u}}_{n+\alpha_m}^w} = \alpha_m \mathbf{I}, \\
\mathbf{K}_{k,(l),\dot{\mathbf{v}}^f} &:= \alpha_f \gamma \Delta t_n \frac{\partial \mathbf{R}_k(\dot{\mathbf{y}}_{n+\alpha_m,(l)}, \mathbf{y}_{n+\alpha_f,(l)})}{\partial \mathbf{v}_{n+\alpha_f}^f} = -\alpha_f \gamma \Delta t_n \mathbf{I}, \\
\mathbf{K}_{k,(l),\dot{\mathbf{p}}^f} &:= \mathbf{0}, \\
\mathbf{K}_{m,(l),\dot{\mathbf{u}}^w} &:= \alpha_f \gamma \Delta t_n \frac{\partial \mathbf{R}_m(\dot{\mathbf{y}}_{n+\alpha_m,(l)}, \mathbf{y}_{n+\alpha_f,(l)})}{\partial \mathbf{u}_{n+\alpha_f}^w}, \\
\mathbf{K}_{m,(l),\dot{\mathbf{v}}^f} &:= \alpha_m \frac{\partial \mathbf{R}_m(\dot{\mathbf{y}}_{n+\alpha_m,(l)}, \mathbf{y}_{n+\alpha_f,(l)})}{\partial \dot{\mathbf{v}}_{n+\alpha_m}^f} + \alpha_f \gamma \Delta t_n \frac{\partial \mathbf{R}_m(\dot{\mathbf{y}}_{n+\alpha_m,(l)}, \mathbf{y}_{n+\alpha_f,(l)})}{\partial \mathbf{v}_{n+\alpha_f}^f}, \\
\mathbf{K}_{m,(l),\dot{\mathbf{p}}^f} &:= \alpha_f \gamma \Delta t_n \frac{\partial \mathbf{R}_m(\dot{\mathbf{y}}_{n+\alpha_m,(l)}, \mathbf{y}_{n+\alpha_f,(l)})}{\partial \mathbf{p}_{n+\alpha_f}^f}, \\
\mathbf{K}_{c,(l),\dot{\mathbf{u}}^w} &:= \mathbf{0}, \\
\mathbf{K}_{c,(l),\dot{\mathbf{v}}^f} &:= \alpha_m \frac{\partial \mathbf{R}_c(\dot{\mathbf{y}}_{n+\alpha_m,(l)}, \mathbf{y}_{n+\alpha_f,(l)})}{\partial \dot{\mathbf{v}}_{n+\alpha_m}^f} + \alpha_f \gamma \Delta t_n \frac{\partial \mathbf{R}_c(\dot{\mathbf{y}}_{n+\alpha_m,(l)}, \mathbf{y}_{n+\alpha_f,(l)})}{\partial \mathbf{v}_{n+\alpha_f}^f}, \\
\mathbf{K}_{c,(l),\dot{\mathbf{p}}^f} &:= \alpha_f \gamma \Delta t_n \frac{\partial \mathbf{R}_c(\dot{\mathbf{y}}_{n+\alpha_m,(l)}, \mathbf{y}_{n+\alpha_f,(l)})}{\partial \mathbf{p}_{n+\alpha_f}^f}.
\end{aligned}$$

The special block structure in the first row of $\mathbf{K}_{(l)}$ can be exploited for the following block decomposition [80, 81],

$$\mathbf{K}_{(l)} = \begin{bmatrix} \mathbf{I} & \mathbf{0} & \mathbf{0} \\ \frac{1}{\alpha_m} \mathbf{K}_{m,(l),\dot{\mathbf{u}}^w} & \mathbf{K}_{m,(l),\dot{\mathbf{v}}^f} + \frac{\alpha_f \gamma \Delta t_n}{\alpha_m} \mathbf{K}_{m,(l),\dot{\mathbf{u}}^w} & \mathbf{K}_{m,(l),\dot{\mathbf{p}}^f} \\ \mathbf{0} & \mathbf{K}_{c,(l),\dot{\mathbf{v}}^f} & \mathbf{K}_{c,(l),\dot{\mathbf{p}}^f} \end{bmatrix} \begin{bmatrix} \alpha_m \mathbf{I} & -\alpha_f \gamma \Delta t_n \mathbf{I} & \mathbf{0} \\ \mathbf{0} & \mathbf{I} & \mathbf{0} \\ \mathbf{0} & \mathbf{0} & \mathbf{I} \end{bmatrix}.$$

With the above decomposition, the original linear system for the Newton-Raphson method,

$$\mathbf{K}_{(l)} \Delta \dot{\mathbf{y}}_{n+1,(l)} = -\mathbf{R}_{(l)},$$

can be solved to obtain the increments $\Delta \dot{\mathbf{y}}_{n+1,(l)} := \{\Delta \dot{\mathbf{u}}_{n+1,(l)}^w, \Delta \dot{\mathbf{v}}_{n+1,(l)}^f, \Delta \dot{\mathbf{p}}_{n+1,(l)}^f\}^T$ at iteration number l in the following two-stage segregated algorithm. In the first stage, intermediate increments are solved from

$$\begin{bmatrix} \mathbf{I} & \mathbf{0} & \mathbf{0} \\ \frac{1}{\alpha_m} \mathbf{K}_{m,(l),\dot{\mathbf{u}}^w} & \mathbf{K}_{m,(l),\dot{\mathbf{v}}^f} + \frac{\alpha_f \gamma \Delta t_n}{\alpha_m} \mathbf{K}_{m,(l),\dot{\mathbf{u}}^w} & \mathbf{K}_{m,(l),\dot{\mathbf{p}}^f} \\ \mathbf{0} & \mathbf{K}_{c,(l),\dot{\mathbf{v}}^f} & \mathbf{K}_{c,(l),\dot{\mathbf{p}}^f} \end{bmatrix} \begin{bmatrix} \Delta \dot{\mathbf{u}}_{n+1,(l)}^{w*} \\ \Delta \dot{\mathbf{v}}_{n+1,(l)}^{f*} \\ \Delta \dot{\mathbf{p}}_{n+1,(l)}^{f*} \end{bmatrix} = - \begin{bmatrix} \mathbf{R}_{k,(l)} \\ \mathbf{R}_{m,(l)} \\ \mathbf{R}_{c,(l)} \end{bmatrix}. \quad (2.51)$$

In the second stage, the increments are obtained from the following system of equations,

$$\begin{bmatrix} \alpha_m \mathbf{I} & -\alpha_f \gamma \Delta t_n \mathbf{I} & \mathbf{0} \\ \mathbf{0} & \mathbf{I} & \mathbf{0} \\ \mathbf{0} & \mathbf{0} & \mathbf{I} \end{bmatrix} \begin{bmatrix} \Delta \dot{\mathbf{u}}_{n+1,(l)}^w \\ \Delta \dot{\mathbf{v}}_{n+1,(l)}^f \\ \Delta \dot{\mathbf{p}}_{n+1,(l)}^f \end{bmatrix} = \begin{bmatrix} \Delta \dot{\mathbf{u}}_{n+1,(l)}^{w*} \\ \Delta \dot{\mathbf{v}}_{n+1,(l)}^{f*} \\ \Delta \dot{\mathbf{p}}_{n+1,(l)}^{f*} \end{bmatrix}. \quad (2.52)$$

From (2.51) and (2.52), we make the following observations,

$$\alpha_m \Delta \dot{\mathbf{u}}_{n+1,(l)}^w - \alpha_f \gamma \Delta t_n \Delta \dot{\mathbf{v}}_{n+1,(l)}^f = \Delta \dot{\mathbf{u}}_{n+1,(l)}^{w*} = -\mathbf{R}_{k,(l)}, \quad \Delta \dot{\mathbf{v}}_{n+1,(l)}^f = \Delta \dot{\mathbf{v}}_{n+1,(l)}^{f*}, \quad \Delta \dot{\mathbf{p}}_{n+1,(l)}^f = \Delta \dot{\mathbf{p}}_{n+1,(l)}^{f*},$$

with which we may reduce the linear systems in the segregated algorithm to

$$\begin{bmatrix} \mathbf{K}_{m,(l),\dot{\mathbf{v}}^f} + \frac{\alpha_f \gamma \Delta t_n}{\alpha_m} \mathbf{K}_{m,(l),\dot{\mathbf{u}}^w} & \mathbf{K}_{m,(l),\dot{\mathbf{p}}^f} \\ \mathbf{K}_{c,(l),\dot{\mathbf{v}}^f} & \mathbf{K}_{c,(l),\dot{\mathbf{p}}^f} \end{bmatrix} \begin{bmatrix} \Delta \dot{\mathbf{v}}_{n+1,(l)}^f \\ \Delta \dot{\mathbf{p}}_{n+1,(l)}^f \end{bmatrix} = - \begin{bmatrix} \mathbf{R}_{m,(l)} - \frac{1}{\alpha_m} \mathbf{K}_{m,(l),\dot{\mathbf{u}}^w} \mathbf{R}_{k,(l)} \\ \mathbf{R}_{c,(l)} \end{bmatrix}, \quad (2.53)$$

$$\Delta \dot{\mathbf{u}}_{n+1,(l)}^w = \frac{\alpha_f \gamma \Delta t_n}{\alpha_m} \Delta \dot{\mathbf{v}}_{n+1,(l)}^f - \frac{1}{\alpha_m} \mathbf{R}_{k,(l)}. \quad (2.54)$$

The segregated algorithm therefore consists of solving (2.53) for $\{\Delta \dot{\mathbf{v}}_{n+1,(l)}^f, \Delta \dot{\mathbf{p}}_{n+1,(l)}^f\}^T$, then subsequently obtaining $\Delta \dot{\mathbf{u}}_{n+1,(l)}^w$ from the algebraic update (2.54). Furthermore, it has been shown in Proposition 5 of [14] that

$$\mathbf{R}_{k,(l)} = \mathbf{0} \quad \text{for } l \geq 2$$

holds true for any given update $\Delta \dot{\mathbf{v}}_{n+1,(l)}^f$ in (2.54), prompting us to set $\mathbf{R}_{k,(l)} = \mathbf{0}$ for all $l \geq 1$ in (2.53). While this may lead to inconsistent updates of $\Delta \dot{\mathbf{v}}_{n+1,(l)}^f$ and $\Delta \dot{\mathbf{p}}_{n+1,(l)}^f$ for $l = 1$, we have observed no deterioration of the overall Newton-Raphson algorithm's convergence rate in our collective experience. Interested readers are referred to Appendix B of [14] for more details on the numerical analysis. For notational simplicity, we denote the block matrices in (2.53) as

$$\mathbf{A}_{(l)} := \mathbf{K}_{m,(l),\dot{\mathbf{v}}^f} + \frac{\alpha_f \gamma \Delta t_n}{\alpha_m} \mathbf{K}_{m,(l),\dot{\mathbf{u}}^w}, \quad \mathbf{B}_{(l)} := \mathbf{K}_{m,(l),\dot{\mathbf{p}}^f}, \quad \mathbf{C}_{(l)} := \mathbf{K}_{c,(l),\dot{\mathbf{v}}^f}, \quad \mathbf{D}_{(l)} := \mathbf{K}_{c,(l),\dot{\mathbf{p}}^f}. \quad (2.55)$$

We can now summarize our above discussion in the following segregated predictor multi-corrector algorithm.

Segregated predictor multi-corrector algorithm

Predictor stage: Set

$$\mathbf{y}_{n+1,(0)} = \mathbf{y}_n, \quad \dot{\mathbf{y}}_{n+1,(0)} = \frac{\gamma - 1}{\gamma} \dot{\mathbf{y}}_n.$$

Multi-corrector stage: Repeat the following steps for $l = 1, 2, \dots, l_{max}$

1. Evaluate the solution vector and its time derivative at intermediate time steps,

$$\mathbf{y}_{n+\alpha_f,(l)} = \mathbf{y}_n + \alpha_f (\mathbf{y}_{n+1,(l-1)} - \mathbf{y}_n), \quad \dot{\mathbf{y}}_{n+\alpha_m,(l)} = \dot{\mathbf{y}}_n + \alpha_m (\dot{\mathbf{y}}_{n+1,(l-1)} - \dot{\mathbf{y}}_n).$$

2. Assemble the residual vector $\mathbf{R}_{(l)}$ using $\dot{\mathbf{y}}_{n+\alpha_m,(l)}$ and $\mathbf{y}_{n+\alpha_f,(l)}$.
3. Let $\|\mathbf{R}_{(l)}\|_{l_2}$ denote the l_2 -norm of the residual vector, and let tol_R and tol_A denote the prescribed relative and absolute tolerances, respectively. If either of the following stopping criteria

$$\frac{\|\mathbf{R}_{(l)}\|_{l_2}}{\|\mathbf{R}_{(0)}\|_{l_2}} \leq \text{tol}_R, \quad \|\mathbf{R}_{(l)}\|_{l_2} \leq \text{tol}_A,$$

is satisfied, then set

$$\mathbf{y}_{n+1} = \mathbf{y}_{n+1,(l-1)}, \quad \dot{\mathbf{y}}_{n+1} = \dot{\mathbf{y}}_{n+1,(l-1)},$$

and exit the multi-corrector stage. Otherwise, continue to step 4.

4. Assemble the following sub-tangent matrices,

$$\begin{aligned}\mathbf{A}_{(l)} &:= \mathbf{K}_{m,(l),\dot{\mathbf{v}}^f} + \frac{\alpha_f \gamma \Delta t_n}{\alpha_m} \mathbf{K}_{m,(l),\dot{\mathbf{u}}^w}, & \mathbf{B}_{(l)} &:= \mathbf{K}_{m,(l),\dot{p}^f}, \\ \mathbf{C}_{(l)} &:= \mathbf{K}_{c,(l),\dot{\mathbf{v}}^f}, & \mathbf{D}_{(l)} &:= \mathbf{K}_{c,(l),\dot{p}^f}.\end{aligned}$$

5. Solve the following linear system for $\Delta \dot{\mathbf{v}}_{n+1,(l)}^f$ and $\Delta \dot{p}_{n+1,(l)}^f$,

$$\begin{bmatrix} \mathbf{A}_{(l)} & \mathbf{B}_{(l)} \\ \mathbf{C}_{(l)} & \mathbf{D}_{(l)} \end{bmatrix} \begin{bmatrix} \Delta \dot{\mathbf{v}}_{n+1,(l)}^f \\ \Delta \dot{p}_{n+1,(l)}^f \end{bmatrix} = - \begin{bmatrix} \mathbf{R}_{m,(l)} \\ \mathbf{R}_{c,(l)} \end{bmatrix}. \quad (2.56)$$

6. Obtain $\Delta \dot{\mathbf{u}}_{n+1,(l)}^w$ from $\Delta \dot{\mathbf{v}}_{n+1,(l)}^f$ via the relation (2.54), that is,

$$\Delta \dot{\mathbf{u}}_{n+1,(l)}^w = \frac{\alpha_f \gamma \Delta t_n}{\alpha_m} \Delta \dot{\mathbf{v}}_{n+1,(l)}^f - \frac{1}{\alpha_m} \mathbf{R}_{k,(l)}.$$

7. Update the solution vector and its time derivative as

$$\mathbf{y}_{n+1,(l)} = \mathbf{y}_{n+1,(l-1)} + \gamma \Delta t_n \Delta \dot{\mathbf{y}}_{n+1,(l)}, \quad \dot{\mathbf{y}}_{n+1,(l)} = \dot{\mathbf{y}}_{n+1,(l-1)} + \Delta \dot{\mathbf{y}}_{n+1,(l)}.$$

In this work, unless otherwise specified, we set the tolerances to $\text{tol}_R = \text{tol}_A = 10^{-6}$ and the maximum number of nonlinear iterations to $l_{max} = 20$.

Remark 9. We have chosen $\mathbf{R}_{k,(l)} = \mathbf{0}$ for all $l \geq 1$ in (2.53) to simplify the formation of the right-hand side of the linear system. We note that the wall displacement update (2.54) still requires a consistent definition of $\mathbf{R}_{k,(l)}$, as stagnation or divergence may otherwise be observed. Numerical evidence will be documented for patient-specific clinical cases in Section 6.3.

Remark 10. In comparison to the consistent tangent matrix for the incompressible Navier-Stokes equations, only block matrix $\mathbf{A}_{(l)}$ has been modified to include the wall stiffness term $\alpha_f \gamma \Delta t_n \mathbf{K}_{m,(l),\dot{\mathbf{u}}^w} / \alpha_m$. As was shown in our prior analysis [51], $\mathbf{A}_{(l)}$ additionally consists of contributions from the transient, convection, viscous, and subgrid scale modeling terms as well as multiple rank-one modifications from coupling with reduced models. Particular attention will thus be paid to approximate $\mathbf{A}_{(l)}$ in our design of the iterative solution method, as discussed in the next section.

Remark 11. We further note that for time steps of practical interest, the use of the ‘frozen-coefficient’ tangent matrix was previously deemed necessary for achieving stability in the first few time steps [44, 82]. Nonetheless, we implement the consistent tangent matrix here as in our previous studies [14, 51, 15] without stability issues, thereby achieving rapid quadratic convergence.

3. Iterative solution method

In this section, we consider the linear system (2.56) arising in the aforementioned segregated predictor multi-corrector algorithm, which often comprises the most time-consuming part of the overall algorithm. We focus on a linear system

$$\mathcal{A} \mathbf{x} = \mathbf{r} \quad (3.1)$$

exhibiting the following 2×2 block structure,

$$\mathcal{A} := \begin{bmatrix} \mathbf{A} & \mathbf{B} \\ \mathbf{C} & \mathbf{D} \end{bmatrix}, \quad \mathbf{x} := \begin{bmatrix} \mathbf{x}_v \\ \mathbf{x}_p \end{bmatrix}, \quad \mathbf{r} := \begin{bmatrix} \mathbf{r}_v \\ \mathbf{r}_p \end{bmatrix}.$$

As is clear from our derivation of the consistent tangent matrix \mathcal{A} in the previous section, the segregated algorithm allows the implicit solver to retain the same block structure as that of the incompressible Navier-Stokes equations [51]. From (2.55), we observe that block matrices \mathbf{B} , \mathbf{C} , and \mathbf{D} are in fact identical to their counterparts in the incompressible Navier-Stokes equations, and the block matrix \mathbf{A} is only modified by an additional term representing the wall contribution, scaled by the time step size and parameters in the generalized- α method. The consistent tangent matrix \mathcal{A} can be factorized as $\mathcal{A} = \mathcal{L}\mathcal{D}\mathcal{U}$, with

$$\mathcal{L} = \begin{bmatrix} \mathbf{I} & \mathbf{O} \\ \mathbf{C}\mathbf{A}^{-1} & \mathbf{I} \end{bmatrix}, \quad \mathcal{D} = \begin{bmatrix} \mathbf{A} & \mathbf{O} \\ \mathbf{O} & \mathbf{S} \end{bmatrix}, \quad \mathcal{U} = \begin{bmatrix} \mathbf{I} & \mathbf{A}^{-1}\mathbf{B} \\ \mathbf{O} & \mathbf{I} \end{bmatrix}, \quad (3.2)$$

where $\mathbf{S} := \mathbf{D} - \mathbf{C}\mathbf{A}^{-1}\mathbf{B}$ is the Schur complement of \mathbf{A} . The above block factorization immediately implies a solution procedure for the linear system $\mathcal{A}\mathbf{x} = \mathbf{r}$. Applying \mathcal{L}^{-1} to both sides of (3.1) transforms the linear system to $\mathcal{D}\mathcal{U}\mathbf{x} = \mathcal{L}^{-1}\mathbf{r}$, which can be written explicitly as

$$\begin{bmatrix} \mathbf{A} & \mathbf{B} \\ \mathbf{O} & \mathbf{S} \end{bmatrix} \begin{bmatrix} \mathbf{x}_v \\ \mathbf{x}_p \end{bmatrix} = \begin{bmatrix} \mathbf{r}_v \\ \mathbf{r}_p - \mathbf{C}\mathbf{A}^{-1}\mathbf{r}_v \end{bmatrix}. \quad (3.3)$$

The so-called Schur complement reduction (SCR) procedure [83, 84] solves (3.3) via back substitution and therefore involves solving smaller systems associated with \mathbf{A} and \mathbf{S} . Given the dense structure of \mathbf{S} stemming from the presence of \mathbf{A}^{-1} , solving a linear system associated with \mathbf{S} to high precision is, however, prohibitively expensive. The SCR procedure can therefore be applied as a preconditioning technique for an iterative solution method, such that the smaller systems need not be solved to high precision. The action of the preconditioner \mathcal{P} for the linear system $\mathcal{A}\mathbf{x} = \mathbf{r}$ is defined in Algorithm 1, where the smaller systems associated with \mathbf{A} and \mathbf{S} are solved by the GMRES algorithm preconditioned by \mathbf{P}_A and \mathbf{P}_S , respectively. The stopping criteria for the two iterative solvers include relative tolerances δ_A and δ_S and maximum iteration numbers n_A^{\max} and n_S^{\max} , respectively.

Algorithm 1 The action of \mathcal{P}^{-1} on a vector $\mathbf{s} := [\mathbf{s}_v; \mathbf{s}_p]^T$ with the output being $\mathbf{y} := [\mathbf{y}_v; \mathbf{y}_p]^T$.

1: Solve for an intermediate velocity $\hat{\mathbf{y}}_v$ from the equation

$$\mathbf{A}\hat{\mathbf{y}}_v = \mathbf{s}_v \quad (3.4)$$

by GMRES preconditioned by \mathbf{P}_A with δ_A and n_A^{\max} prescribed.

2: Update the continuity residual by $\mathbf{s}_p \leftarrow \mathbf{s}_p - \mathbf{C}\hat{\mathbf{y}}_v$.

3: Solve for \mathbf{y}_p from the equation

$$\mathbf{S}\mathbf{y}_p = \mathbf{s}_p \quad (3.5)$$

by GMRES preconditioned by \mathbf{P}_S with δ_S and n_S^{\max} prescribed. \triangleright The action of \mathbf{S} on a vector in the GMRES iteration will be defined in Algorithm 2.

4: Update the momentum residual by $\mathbf{s}_v \leftarrow \mathbf{s}_v - \mathbf{B}\mathbf{y}_p$.

5: Solve for \mathbf{y}_v from the equation

$$\mathbf{A}\mathbf{y}_v = \mathbf{s}_v \quad (3.6)$$

by GMRES preconditioned by \mathbf{P}_A with δ_A and n_A^{\max} prescribed.

Since the preconditioner \mathcal{P} is defined through an algorithm, its algebraic definition may vary over iterations. The flexible GMRES (FGMRES) algorithm [85] is thus applied as the outer iterative method for the tangent matrix \mathcal{A} with a corresponding relative tolerance δ and maximum iteration number n^{\max} . In this work, we set the relative tolerances $\delta_A = 10^{-5}$, $\delta_S = 10^{-2}$ and maximum iteration numbers $n_A^{\max} = n_S^{\max} = 100$, $n^{\max} = 200$ unless otherwise specified. While the FGMRES algorithm minimizes the residual over the

generated subspace, its convergence is not guaranteed in general, as the approximation subspace is not a standard Krylov subspace. Nonetheless, given this flexibility in preconditioner variation over iterations, the robustness and efficiency of the overall iterative method can be well balanced with a proper design of \mathcal{P} . We therefore turn our attention to the design of \mathbf{P}_A and \mathbf{P}_S for the associated GMRES algorithms.

The block matrix \mathbf{A} consists of a discrete convection-diffusion-reaction operator, subgrid scale modeling terms, rank-one modifications from reduced models coupled to the outflow boundaries to represent the downstream vasculature [51] (see also Section 5.3), and the stiffness matrix of the vascular wall (see (2.55)). The class of multigrid methods, which has been proposed as a scalable and robust preconditioner for elliptic problems [86], presents an attractive choice for \mathbf{P}_A , particularly when the mesh size demands extremely large-scale parallel computations. Compared to the geometric multigrid method [87], the algebraic multigrid method (AMG) can more conveniently be integrated with numerical codes developed for unstructured grids.

The Schur complement \mathbf{S} is implicitly defined through the four block matrices. While constructing and storing \mathbf{S} is rather cost-prohibitive, the GMRES algorithm only necessitates the construction of a Krylov subspace via repeated matrix-vector multiplication operations. The action of \mathbf{S} on a given vector can therefore be computed with the four block matrices on the fly in a so-called “matrix-free” fashion as outlined in Algorithm 2, which is used to construct the Krylov subspace in Step 3 of Algorithm 1. Inspired by the SIMPLE algorithm, the preconditioner \mathbf{P}_S is formed by BoomerAMG [88] based on a sparse approximation of \mathbf{S} given by $\hat{\mathbf{S}} := \mathbf{D} - \mathbf{C}(\text{diag}(\mathbf{A}))^{-1}\mathbf{B}$.

Algorithm 2 The matrix-free algorithm for multiplying \mathbf{S} with a vector \mathbf{x}_p .

- 1: Compute the matrix-vector multiplication $\hat{\mathbf{x}}_p \leftarrow \mathbf{D}\mathbf{x}_p$.
- 2: Compute the matrix-vector multiplication $\bar{\mathbf{x}}_p \leftarrow \mathbf{B}\mathbf{x}_p$.
- 3: Solve for $\tilde{\mathbf{x}}_p$ from the linear system

$$\mathbf{A}\tilde{\mathbf{x}}_p = \bar{\mathbf{x}}_p \tag{3.7}$$

by GMRES preconditioned by \mathbf{P}_A with δ_I and n_A^{\max} prescribed.

▷ The action of \mathbf{A}^{-1} on $\bar{\mathbf{x}}_p$ is approximated by solving (3.7) with the given stopping criteria.

- 4: Compute the matrix-vector multiplication $\bar{\mathbf{x}}_p \leftarrow \mathbf{C}\tilde{\mathbf{x}}_p$.
 - 5: **return** $\hat{\mathbf{x}}_p - \bar{\mathbf{x}}_p$.
-

We note that replacing equation (3.5) in Algorithm 1 by $\hat{\mathbf{S}}\mathbf{y}_p = \mathbf{s}_p$ renders the FGMRES algorithm similar to the SIMPLE algorithm, which does not require solving equation (3.7). The preconditioner stated in Algorithm 1 may therefore be regarded as a generalization of the SIMPLE algorithm, in which the matrix-free algorithm stated in Algorithm 2 is invoked to attain an improved approximation of the Schur complement.

Remark 12. *The matrix-free technique is often invoked in Krylov subspace methods when assembling or storing a matrix is inconvenient or expensive. Often, a sparse approximation to the unassembled matrix, like $\hat{\mathbf{S}}$, is also designed to provide a preconditioner to accelerate the Krylov iteration. This approach can also be found in higher-order methods [89, 90] and Jacobian-free nonlinear solvers [91].*

4. Verification by the Womersley solution

In this section, we present two verification studies using the Womersley solutions describing pulsatile flow in an axisymmetric cylindrical pipe, first with rigid walls and subsequently with thin, linear elastic walls. Furthermore, in the case of the rigid pipe, we use analytical solutions for pressure, velocity, and wall shear stress (WSS) to perform spatial convergence studies. All parameters are reported in centimeter-gram-second units in this work.

4.1. Womersley flow in a rigid pipe

The Womersley solution for pulsatile flow in a rigid pipe describes axisymmetric, fully developed flow subject to a pressure gradient with both steady and oscillatory contributions. The pressure can be expressed with the following Fourier series,

$$p = p_{\text{ref}} + \left(k_0 + \sum_{n=1}^N k_n e^{\iota n \omega t} \right) z, \quad (4.1)$$

where z is the longitudinal coordinate along the length of the pipe, p_{ref} is the reference pressure at the $z = 0$ surface, k_0 is the steady zeroth mode of the pressure gradient, k_n is the n -th Fourier coefficient in the oscillatory component of the pressure gradient, ι is the solution to $\iota^2 = -1$, T_p is the period of oscillation, and $\omega := 2\pi/T_p$ is the fundamental frequency. Whereas k_0 produces steady forward flow, the oscillatory component of the pressure gradient drives a phase-shifted oscillatory flow with zero net flow over T_p . Per the assumptions of axisymmetric and fully developed flow, the velocity is identically zero in the radial and circumferential directions and takes the following analytical form in the axial direction,

$$v_z = \frac{k_0}{4\mu^f} (r^2 - R^2) + \sum_{n=1}^N \frac{\iota k_n}{\rho^f n \omega} \left(1 - \frac{J_0(\iota^{\frac{3}{2}} \alpha_n \frac{r}{R})}{J_0(\iota^{\frac{3}{2}} \alpha_n)} \right) e^{\iota n \omega t}, \quad (4.2)$$

wherein $r := \sqrt{x^2 + y^2}$, R is the pipe radius, J_0 is the zeroth-order Bessel function of the first kind, and $\alpha_n := R\sqrt{\rho^f n \omega / \mu^f}$ is the Womersley number for the n -th Fourier mode. The only nonzero component of WSS takes the corresponding form,

$$\tau_{zr} = \sigma_{\text{dev}, zr}^f|_{r=R} = \frac{k_0 R}{2} - \sum_{n=1}^N \frac{k_n R}{\iota^{\frac{3}{2}} \alpha_n} \frac{J_1(\iota^{\frac{3}{2}} \alpha_n)}{J_0(\iota^{\frac{3}{2}} \alpha_n)} e^{\iota n \omega t}. \quad (4.3)$$

The complex forms of p , v_z , and τ_{zr} in (4.1)-(4.3) indicate the existence of two sets of real independent solutions. Here, we take the set of real components as the benchmark solution and represent a single oscillatory mode (i.e., $N = 1$).

To reflect typical physiological flows, we set the pipe radius R to 0.3; fluid density ρ^f and viscosity μ^f to 1.0 and 0.04, respectively; period T_p to 1.1; reference pressure p_{ref} to 0; and Fourier coefficients k_0 and k_1 to -21.0469 and $-33.0102 + 42.9332\iota$, respectively. Correspondingly, the fundamental frequency ω and Womersley number α_1 were approximately 5.71 and 3.59, respectively. Furthermore, given the fully developed flow, we set a short pipe length of 0.3. The no-slip boundary condition was prescribed on the wall, and traction boundary conditions were prescribed on both the inlet and outlet. Simulations were performed with uniform time steps using both linear (P1) and quadratic (P2) tetrahedral meshes of comparable numbers of nodes generated by MeshSim (Simmetrix, Inc., Clifton Park, NY, USA), and relative errors of velocity, pressure, and WSS were computed. To circumvent confounding errors from temporal discretization, temporal refinement was performed for each simulation until the first three significant digits of all computed errors were preserved across two temporal refinement levels.

Figure 1 plots the relative errors of velocity \mathbf{v}_h and WSS $\boldsymbol{\tau}_h$ in the L_2 norm, and of pressure p_h in the L_2 and H_1 norms. For three of the four computed errors (Figure 1 A, B, and D), we consistently observe theoretical rates, with P2 elements exhibiting spatial accuracy of one order higher than that of P1 elements. For P2 elements, however, the relative error of p_h in the L_2 norm (Figure 1 C), converges faster than the theoretical rate of 2.5. This is likely due to the fact that the analytical solution for pressure here is only linear in space and thus falls within a subspace smaller than the approximation space.

4.2. Womersley flow in a thin-walled elastic pipe

As in the rigid case, the Womersley solution for pulsatile flow in an elastic pipe describes axisymmetric flow subject to a pressure gradient with both steady and oscillatory contributions. Given the motion of the elastic pipe, however, the radial velocity of the fluid is no longer identically zero, and the pressure

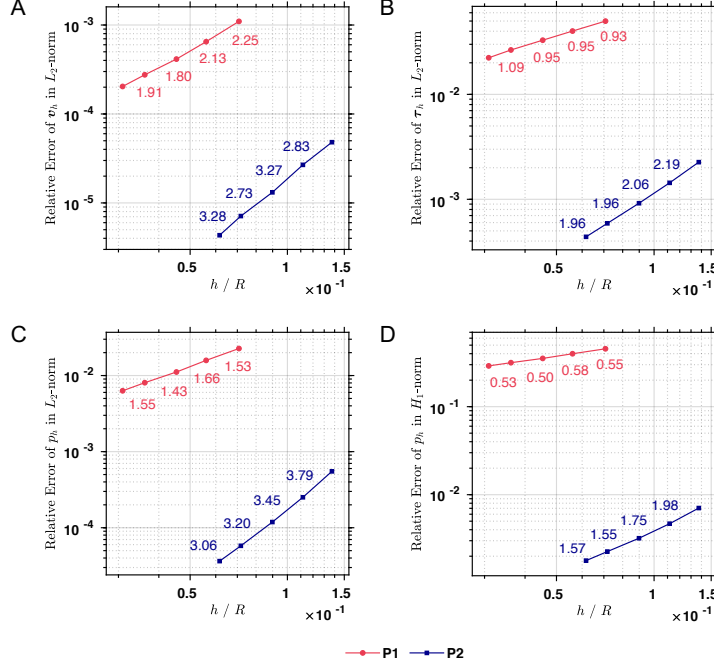


Figure 1: Relative errors of (A) v_h in L_2 norm, (B) τ_h in L_2 norm, (C) p_h in L_2 norm, and (D) p_h in H_1 norm for linear (P1) and quadratic (P2) tetrahedral elements with different mesh sizes h normalized by the pipe radius R . Convergence rates computed from successive errors and mesh sizes are annotated.

propagates down the pipe with a gradient dependent on both time t and the longitudinal coordinate z . This wave propagation is in sharp contrast to the rigid case, in which the fluid oscillates in bulk.

Let c_n be the n -th complex-valued wave speed. Then under the long-wave approximation, namely that the wavelength $\lambda_n := c_n T_p = 2\pi c_n / (n\omega)$ is much larger than the pipe radius R , and the assumption that the wave speed c_n is much larger than the fluid velocity, all nonlinear convective terms can be considered negligible, thereby reducing the Navier-Stokes equations to a set of linear equations. As in the rigid case in Section 4.1, the solution can then be represented as the summation of N superimposed Fourier series. In this case, pressure can be expressed with Fourier coefficients B_n as follows,

$$p = p_{\text{ref}} + B_0 z + \sum_{n=1}^N B_n e^{i n \omega (t - z/c_n)}, \quad (4.4)$$

In addition to a thin-walled assumption for the elastic pipe (i.e., $h^s \ll R$), the radial wall displacement can be assumed small such that the continuity of velocity at the fluid-solid interface can be imposed at the neutral position of the wall, $r = R$. The fluid velocity components in the longitudinal and radial directions, v_z and v_r , can then be expressed with the same Fourier coefficients B_n ,

$$v_z = \frac{B_0}{4\mu^f} (r^2 - R^2) + \sum_{n=1}^N \frac{B_n}{\rho^f c_n} \left(1 - G_n \frac{J_0(\iota^{\frac{3}{2}} \alpha_n \frac{r}{R})}{J_0(\iota^{\frac{3}{2}} \alpha_n)} \right) e^{i n \omega (t - z/c_n)}, \quad (4.5)$$

$$v_r = \sum_{n=1}^N \frac{i n \omega B_n R}{2\rho^f c_n^2} \left(\frac{r}{R} - G_n \frac{2J_1(\iota^{\frac{3}{2}} \alpha_n \frac{r}{R})}{\iota^{\frac{3}{2}} \alpha_n J_0(\iota^{\frac{3}{2}} \alpha_n)} \right) e^{i n \omega (t - z/c_n)}, \quad (4.6)$$

and the wall displacement components in the longitudinal and radial directions, u_z and u_r , are

$$u_z = \sum_{n=1}^N \frac{\iota B_n}{\rho^f c_n n \omega} (G_n - 1) e^{\iota n \omega (t - z/c_n)}, \quad u_r = \sum_{n=1}^N \frac{B_n R}{2 \rho^f c_n^2} (1 - G_n g_n) e^{\iota n \omega (t - z/c_n)}. \quad (4.7)$$

The volumetric flow rate can be found by integrating v_z over a cross-section of the pipe,

$$Q = \int_0^R 2\pi r v_z dr = \frac{-\pi B_0 R^4}{8\mu^f} + \sum_{n=1}^N \frac{B_n \pi R^2}{\rho^f c_n} (1 - G_n g_n) e^{\iota n \omega (t - z/c_n)}. \quad (4.8)$$

In the above analytical forms, G_n is the elasticity factor defined as

$$G_n := \frac{2 + \gamma_n(2\nu - 1)}{\gamma_n(2\nu - g_n)}, \quad \gamma_n := \frac{E h^s}{\rho^f R(1 - \nu^2) c_n^2},$$

and the wave speed c_n can be determined from the following equation,

$$(g_n - 1)(\nu^2 - 1)\gamma_n^2 + \left(\frac{\rho^s h^s}{\rho^f R} (g_n - 1) + (2\nu - 0.5)g_n - 2 \right) \gamma_n + \frac{2\rho^s h^s}{\rho^f R} + g_n = 0, \quad (4.9)$$

wherein

$$g_n := \frac{2J_1(\iota^{\frac{3}{2}} \alpha_n)}{\iota^{\frac{3}{2}} \alpha_n J_0(\iota^{\frac{3}{2}} \alpha_n)}.$$

Equation (4.9), commonly known as the frequency equation, is constructed by demanding a nontrivial solution to the coupled system of the fluid and elastic pipe [27, Sec. 5.7]. Upon solving for γ_n from (4.9), c_n can be represented as

$$c_n = \sqrt{\frac{2}{(1 - \nu^2)\gamma_n}} c_{\text{inv}},$$

where c_{inv} is the wave speed in inviscid flows, as given by the Moens-Korteweg formula,

$$c_{\text{inv}} = \sqrt{\frac{E h^s}{2\rho^f R}}. \quad (4.10)$$

The consequence of this complex-valued wave speed c_n can be understood from the following decomposition,

$$\frac{1}{c_n} = \frac{1}{c_n^{\text{R}}} + \iota \frac{1}{c_n^{\text{I}}}, \quad c_n^{\text{R}} := (\text{Re}[c_n^{-1}])^{-1}, \quad c_n^{\text{I}} := (\text{Im}[c_n^{-1}])^{-1},$$

wherein c_n^{R} and c_n^{I} are commonly referred to as the dispersion and attenuation coefficients, respectively representing differences in the wave frequency and amplitude from the inviscid case. As is clear from above, c_n depends not only on properties of the fluid and the pipe, but also on the frequency of oscillations.

We again considered only the real components as the benchmark solution and represented a single oscillatory mode ($N = 1$). As in Section 4.1, we set the pipe radius R to 0.3, fluid density ρ^f to 1.0, viscosity μ^f to 0.04, period T_p to 1.1, and reference pressure p_{ref} to 0. We further set the pipe length L to 15, and considered uniform wall properties, including a wall density ρ^s of 1.0, Poisson's ratio ν of 0.5, thickness h^s of 0.06, and Young's modulus E of 9.5678×10^6 , which yielded a wave speed c_1 of $886.31 + 29.786\iota$. In order to achieve the same volumetric flow rate as in Section 4.1, the Fourier coefficients B_0 and B_1 were set to -21.0469 and $-4926.29 - 4092.54\iota$, respectively. Given these parameters, we may examine the validity of the invoked assumptions. At the fundamental frequency, the real component of the wave speed $c_1^{\text{R}} = 887.31$ is much larger than the maximum longitudinal velocity $\max\{v_z\} = 21.0701$. Correspondingly, the real

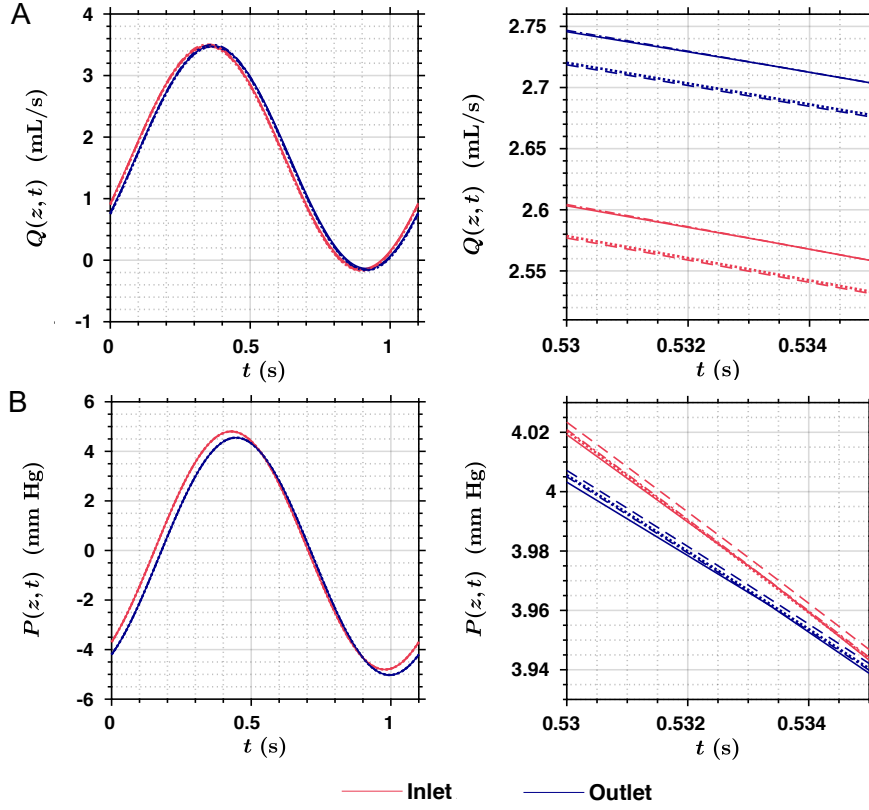


Figure 2: Analytical (solid) and numerical solutions from CMM (dashed) and our reduced unified continuum formulation using either P1 (dotted) or P2 (dash-dotted) elements for the inlet and outlet (A) volumetric flow rates and (B) pressures over a period. Detailed views are shown in the right column.

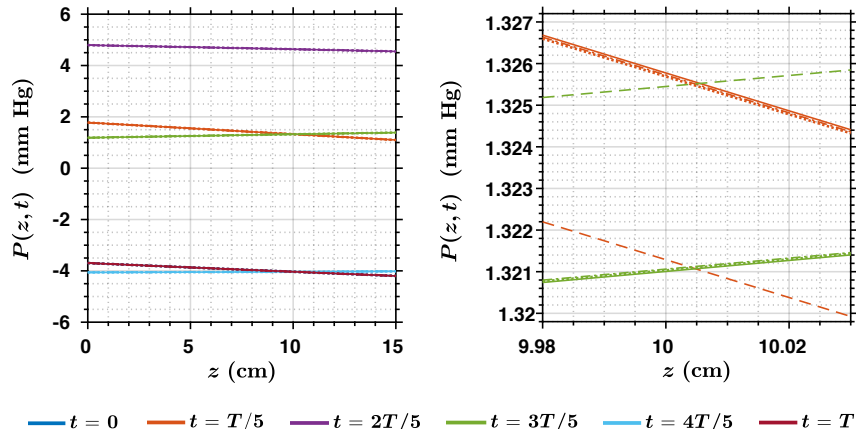
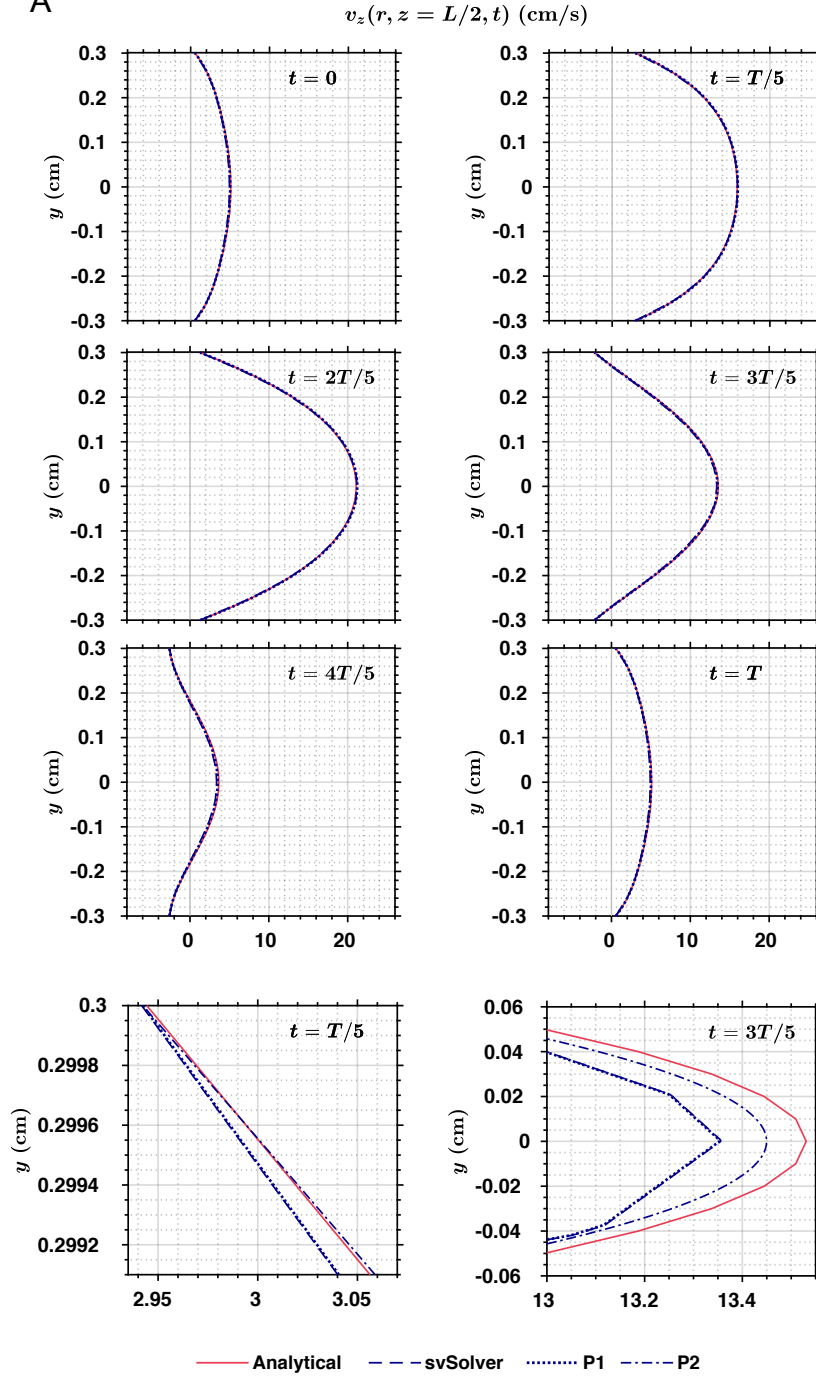


Figure 3: Analytical (solid) and numerical solutions from CMM (dashed) and our reduced unified continuum formulation using either P1 (dotted) or P2 (dash-dotted) elements for the pressures along the longitudinal axis at different time instances. The solutions at $t = 0$ and $t = T$ are overlaid as a result of temporal periodicity. A detailed view is shown on the right.

A



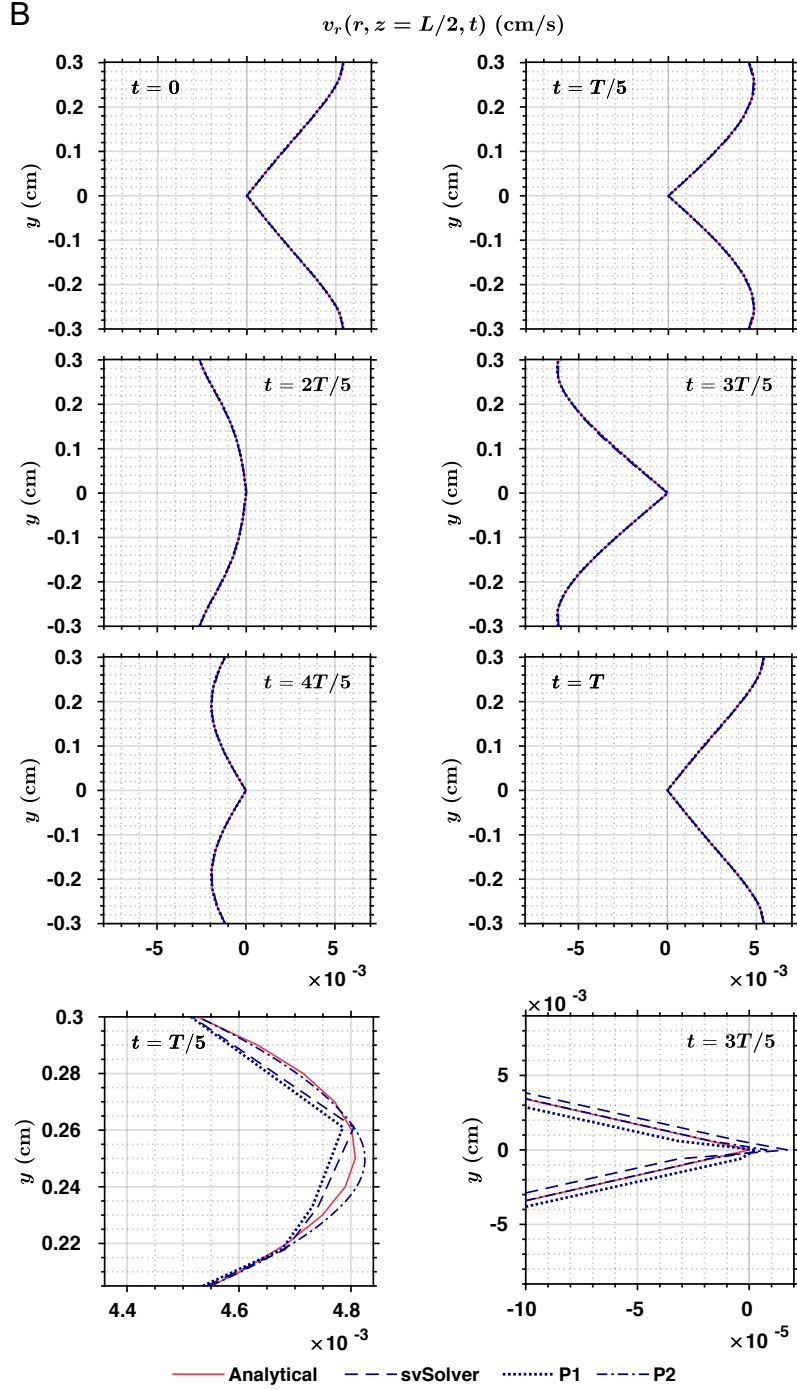


Figure 4: Analytical and numerical solutions from CMM (dashed) and our reduced unified continuum formulation using either P1 or P2 elements for the (A) longitudinal and (B) radial velocity profiles along the y -axis on the $z = L/2$ surface at different time instances. Detailed views at $t = T/5$ and $t = 3T/5$ are shown in the bottom row.

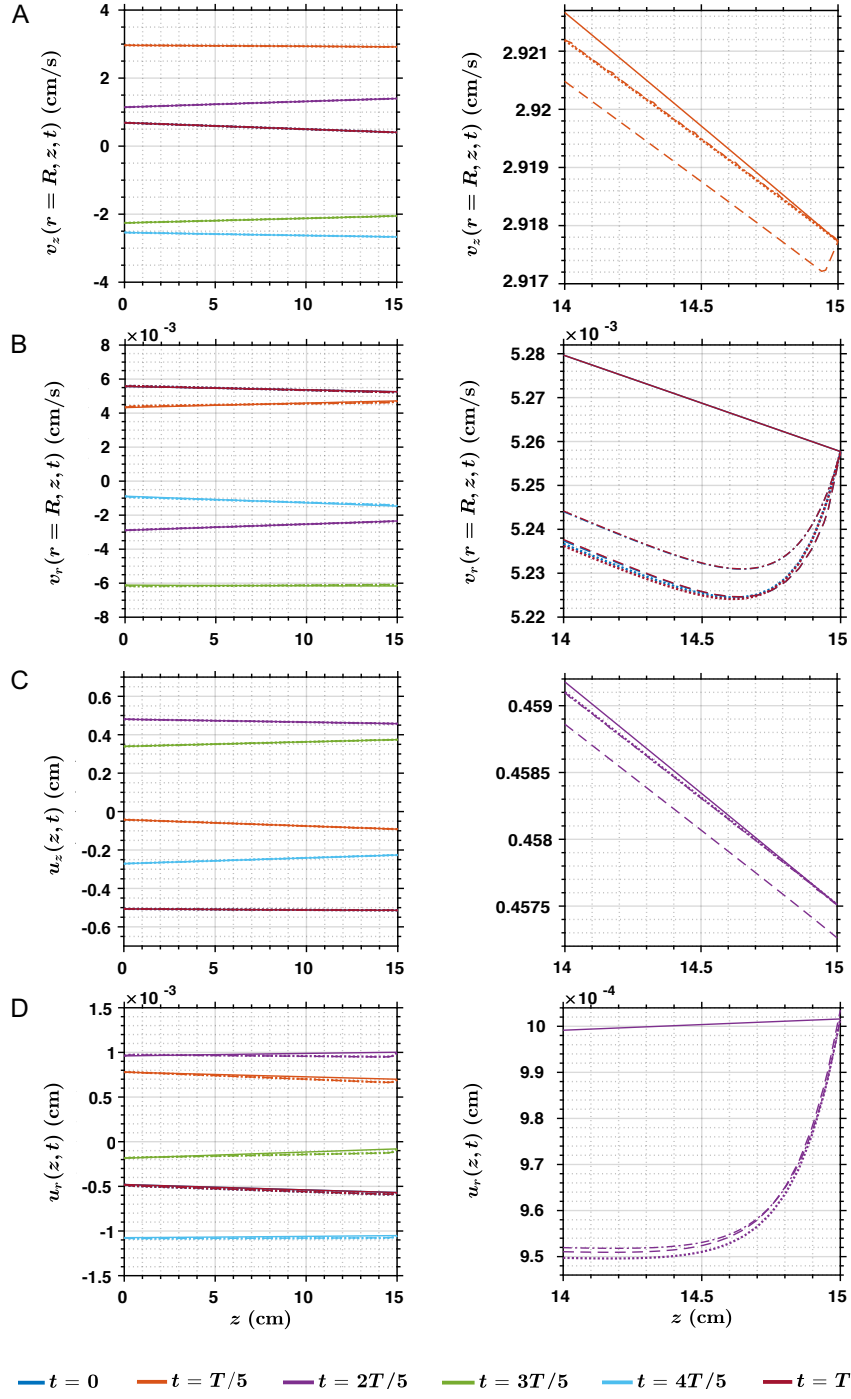


Figure 5: Analytical (solid) and numerical solutions from CMM (dashed) and our reduced unified continuum formulation using either P1 (dotted) or P2 (dash-dotted) elements for the (A) longitudinal and (B) radial fluid velocities at the wall, and the (C) longitudinal and (D) radial wall displacements along the longitudinal axis at different time instances. The solutions at $t = 0$ and $t = T$ are overlaid as a result of temporal periodicity. Detailed views are shown in the right column.

component of the leading wavelength $\lambda_1^R := c_1^R T_p = 2\pi c_1^R / \omega$ is 976.05, three orders of magnitude larger than $R = 0.3$, thereby satisfying the long wave approximation assumption. We further verify for the elastic pipe that both the thickness $h^s = 0.06$ and the maximum radial wall displacement $\max\{u_r\} = 0.0010$ are much smaller than R .

To account for the truncation of the semi-infinite domain used in Womersley's derivation to a finite domain, Cartesian velocity components were prescribed on the boundary nodes of the wall at $z = 0$ and $z = L$ in the following form,

$$\mathbf{v}|_{r=R} := \{v_x, v_y, v_z\}|_{r=R} = \{v_r \cos\theta, v_r \sin\theta, v_z\}|_{r=R},$$

wherein θ is the four-quadrant inverse tangent of the point (x, y) .¹ Traction boundary conditions were prescribed on both the inlet and outlet surfaces, where the traction \mathbf{h}^f was constructed from the pressure in (4.1) and the following Cartesian velocity gradients,

$$\begin{aligned} \frac{\partial v_x}{\partial x} &= \cos^2\theta \frac{\partial v_r}{\partial r} + \frac{\sin^2\theta}{r} v_r, & \frac{\partial v_x}{\partial y} &= \sin\theta \cos\theta \left(\frac{\partial v_r}{\partial r} - \frac{v_r}{r} \right), & \frac{\partial v_x}{\partial z} &= \cos\theta \frac{\partial v_r}{\partial z}, \\ \frac{\partial v_y}{\partial x} &= \sin\theta \cos\theta \left(\frac{\partial v_r}{\partial r} - \frac{v_r}{r} \right), & \frac{\partial v_y}{\partial y} &= \sin^2\theta \frac{\partial v_r}{\partial r} + \frac{\cos^2\theta}{r} v_r, & \frac{\partial v_y}{\partial z} &= \sin\theta \frac{\partial v_r}{\partial z}, \\ \frac{\partial v_z}{\partial x} &= \cos\theta \frac{\partial v_z}{\partial r}, & \frac{\partial v_z}{\partial y} &= \sin\theta \frac{\partial v_z}{\partial r}, & \frac{\partial v_z}{\partial z} &= \frac{\partial v_z}{\partial z}, \end{aligned}$$

wherein

$$\begin{aligned} \frac{\partial v_z}{\partial r} &= \frac{B_0 r}{2\mu^f} + \sum_{n=1}^N \frac{\iota^{\frac{3}{2}} \alpha_n B_n G_n J_1(\iota^{\frac{3}{2}} \alpha_n \frac{r}{R})}{\rho^f c_n J_0(\iota^{\frac{3}{2}} \alpha_n)} e^{\iota n \omega (t - z/c_n)}, \\ \frac{\partial v_z}{\partial z} &= \sum_{n=1}^N \frac{-\iota n \omega B_n}{\rho^f c_n^2} \left(1 - G_n \frac{J_0(\iota^{\frac{3}{2}} \alpha_n \frac{r}{R})}{J_0(\iota^{\frac{3}{2}} \alpha_n)} \right) e^{\iota n \omega (t - \frac{z}{c_n})}, \\ \frac{\partial v_r}{\partial r} &= \sum_{n=1}^N \frac{\iota n \omega_n B_n}{2\rho^f c_n^2} \left(1 - G_n \frac{2 \left(J_1(\iota^{\frac{3}{2}} \alpha_n \frac{r}{R}) - J_2(\iota^{\frac{3}{2}} \alpha_n \frac{r}{R}) \right)}{\iota^{\frac{3}{2}} \alpha_n \frac{r}{R} J_0(\iota^{\frac{3}{2}} \alpha_n)} \right) e^{\iota n \omega (t - z/c_n)}, \\ \frac{\partial v_r}{\partial z} &= \sum_{n=1}^N \frac{n^2 \omega^2 B_n R}{2\rho^f c_n^3} \left(\frac{r}{R} - G_n \frac{2J_1(\iota^{\frac{3}{2}} \alpha_n \frac{r}{R})}{\iota^{\frac{3}{2}} \alpha_n J_0(\iota^{\frac{3}{2}} \alpha_n)} \right) e^{\iota n \omega (t - z/c_n)}. \end{aligned}$$

We note that our choice of boundary conditions differs from the approach adopted in verification studies for CMM, in which only the normal components of the tractions are prescribed on the inlet and outlet surfaces via impedance boundary conditions [40, 41].

Simulations were performed over three periods with uniform time steps using linear and quadratic tetrahedral meshes, both of 284,400 elements and respectively 53,879 and 404,473 nodes. The linear tetrahedral mesh was additionally used to make comparisons against svSolver [92], the CMM implementation in Sim-Vascular. For each simulation, only the final period was analyzed. Given the assumptions and scaling analyses invoked in the derivations, the analytical solutions (4.5)-(4.7) are only approximate solutions to the FSI problem presented in Section 2 and thereby preclude any spatial convergence analyses. We show comparisons of analytical and numerical solutions for the volumetric flow rates and pressures (Figures 2, 3), longitudinal and radial fluid velocity profiles (Figure 4), and longitudinal and radial wall velocity and displacement (Figure 5). We note that all numerical results are nearly indistinguishable from the analytical solutions. Differences, however, can be observed in the detailed views, where the P2 results are in closer agreement to the analytical solutions compared to the P1 results. In Figures 2B and 3, we observe that

¹This function is commonly denoted as $\theta := \text{atan2}(y, x)$ in programming languages.

CMM yields larger discrepancies in pressure than our proposed method, likely due to the different treatment of pressure in the temporal discretization (see Remark 8) [49]. Across all numerical cases, the fluid velocity is in good agreement with the analytical solutions and presents axisymmetric profiles along the radial direction. This is in sharp contrast to existing CMM verification results in the literature exhibiting a notable lack of axisymmetry in the radial velocity profiles [41] that could be attributed to the outlet impedance boundary condition [40, 41], which neglects viscous traction components. Contrary to the fluid quantities, larger discrepancies can be observed in the wall displacement and velocity. These discrepancies, which were not mitigated upon mesh refinement, can be attributed to the assumptions inherent in the theory.

5. Physiological modeling techniques

In this section, we briefly present a suite of practical techniques for appropriate modeling of physiological phenomena in clinical applications. Specifically, these techniques pertain to vascular wall thickness heterogeneity, in vivo tissue prestressing, and boundary conditions reflecting distal vasculature.

5.1. Spatially varying vascular wall thickness

The most commonly employed imaging modalities, such as computed tomography or magnetic resonance angiography, do not adequately resolve vascular wall thicknesses for most applications of clinical interest. While intravascular ultrasound is a notable exception, it is only performed in a small subset of clinical cases, primarily in the coronary vasculature. As a result, spatially varying distributions of vascular wall thicknesses must frequently be prescribed with limited knowledge, commonly with an assumed local thickness-to-radius ratio [93]. In a previously proposed Laplacian approach [57], a Laplacian problem is solved with prescribed Dirichlet boundary conditions at the wall boundary nodes on all inlets and outlets [57]. A similar approach has also since been adopted for prescribing cardiac fiber orientations in heart models [94]. While the Laplacian approach effectively generates smooth distributions of wall thicknesses, it fails to capture sharp local changes in geometry as often occur in disease, yielding physiological thicknesses near the inlets and outlets but significant deviations from the desired thickness-to-radius ratio elsewhere. For example, non-physiological wall thicknesses up to 134% of the local radii are prescribed in the coronary arteries near the ostia on the aortic root (Figure 6B).

For more refined control over the local thickness, we instead adopt a centerline-based approach similar to the one used in [95], in which centerlines for all inlet-outlet pairs are extracted using the Vascular Modeling Toolkit [96, 97]. Upon specifying a global distribution over the entire wall, we can overwrite thicknesses with distinct local distributions for arbitrary sub-domains of the wall. We summarize our approach in Algorithm 3, in which the conglomeration of all vessel centerlines is referred to as the *global centerline*. We note that for geometries with sharp changes in radius, simply computing the local radius as the shortest distance to the global centerline could yield values based not on the corresponding vessel centerline of interest, but rather on an alternate centerline adjoined to the vessel centerline of interest. It is therefore sometimes helpful to extract individual vessel-specific centerlines from the global centerline prior to overwriting thicknesses in vessel sub-domains. In this work, we set a thickness-to-radius ratio of 20% [93], which is precisely satisfied everywhere (Figure 6B).

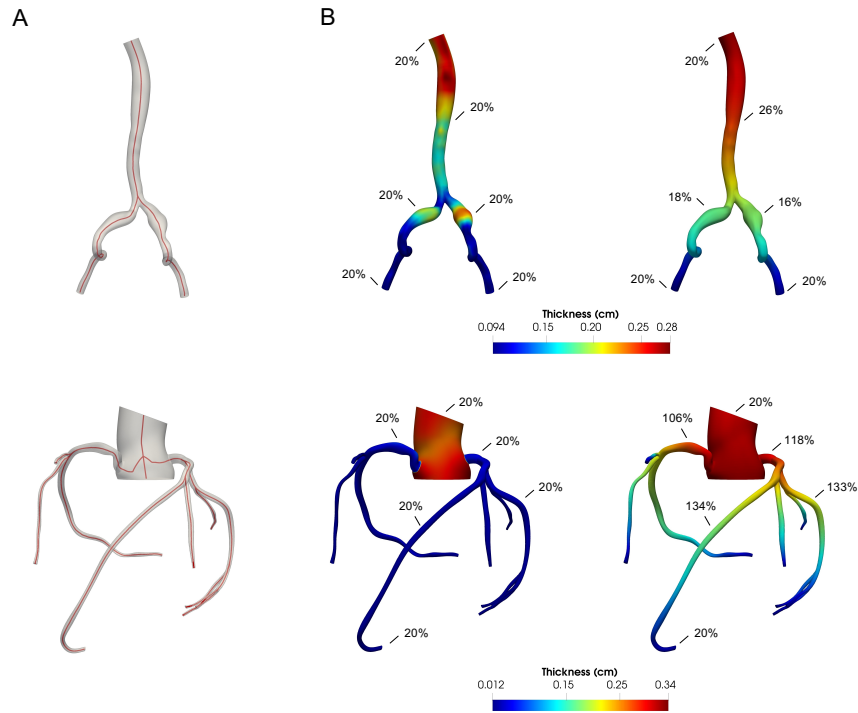


Figure 6: (A) Centerlines extracted for healthy models of the aortailiac (top) and coronary arteries (bottom). (B) Spatially varying wall thickness distributions obtained from the centerline-based (left) and Laplacian (right) approaches. The wall thickness is precisely 20% of the local radius *everywhere* in the centerline-based approach, but *only at the inlets and outlets* in the Laplacian approach. Local thickness-to-radius ratios are annotated at multiple sites to highlight the Laplacian approach's deviation from the prescribed thickness-to-radius ratio and its resulting non-physiological wall thickness distribution.

Algorithm 3 Centerline-based assignment of spatially varying vascular wall thickness.

```

1: Extract the global centerline from the wall surface [98]
2: for each node on the wall do
3:   Compute the radius  $r$  as the shortest distance to the global centerline
4:   Compute the thickness  $h^s \leftarrow x\% r$ 
5: end for
6: for each sub-domain with a distinct local distribution do
7:   Extract the local centerline from the global centerline
8:   for each node on the sub-domain do
9:     Compute the radius  $r$  as the shortest distance to the local centerline
10:    Compute the thickness  $h^s$  as desired
11:   end for
12: end for

```

5.2. Tissue prestressing

The semi-discrete FSI formulation (2.42)-(2.44) assumes the in vivo vascular wall configuration at imaging to be stress-free, yet vascular walls withstand physiological loading. An internal stress state, termed the prestress, must exist to balance the in vivo blood pressure and viscous traction. In contrast to approaches that seek to determine a stress-free configuration [99, 25], here we generate the prestress σ_0 via a fixed-point algorithm similar to the one proposed for an ALE formulation [100, 101]. Given a prestress field σ_0 , the wall momentum balance (2.41) in the FSI formulation can correspondingly be modified as

$$\begin{aligned} \mathbf{B}_m^w(\mathbf{w}_h^f; \dot{\mathbf{y}}_h, \mathbf{y}_h) &:= \int_{\Gamma_I} \mathbf{w}_h^f \cdot \rho^s h^s \left(\frac{d\mathbf{v}_h^f}{dt} - \mathbf{b}^s \right) d\Gamma + \int_{\Gamma_I} h^s \epsilon(\mathbf{w}_h^f) : (\sigma^s(\mathbf{u}_h^w) + \sigma_0) d\Gamma \\ &\quad - \int_{\partial\Gamma_I \cap \Gamma_s^h} h^s \mathbf{w}_h^f \cdot \mathbf{h}^s d\Gamma. \end{aligned} \quad (5.1)$$

To determine σ_0 , we consider the following variational problem for the vascular wall. Given the body force per unit mass \mathbf{b}^s , boundary traction \mathbf{h}^s , and fluid boundary traction \mathbf{h}^f , find $\mathbf{u}_h^w \in \mathcal{S}_u^w$ and $\mathbf{v}_h^w \in \mathcal{S}_v^w$, such that for $\forall \mathbf{w}_h^f \in \mathcal{V}_v^f$,

$$\mathbf{0} = \frac{d\mathbf{u}_h^w}{dt} - \mathbf{v}_h^w, \quad \text{and} \quad \mathbf{0} = \mathbf{B}_m^w(\mathbf{w}_h^f; \dot{\mathbf{y}}_h, \mathbf{y}_h) + \int_{\Gamma_I} \mathbf{w}_h^f \cdot \mathbf{h}^f d\Gamma, \quad (5.2)$$

where \mathcal{S}_u^w and \mathcal{V}_v^f are as previously defined in Section 2.2, and \mathcal{S}_v^w is a suitable trial solution space for the wall velocity. Using the prestress generation algorithm summarized below, σ_0 is then determined such that equations (5.2) are satisfied under the imaged wall configuration. We denote the prestress at the m -th iteration as $\sigma_{0,(m)}$ and the maximum number of iterations as m_{\max} .

Prestress generation algorithm

Initialization: Set $\sigma_{0,(0)} = \mathbf{0}$ and $\mathbf{u}_0^w = \mathbf{0}$.

Fixed-point iteration: Repeat the following steps for $m = 0, 1, \dots, m_{\max}$.

1. Set $\sigma_0 = \sigma_{0,(m)}$ and $\mathbf{u}_m^w = \mathbf{0}$.
2. From t_m to t_{m+1} , solve the variational problem (5.2) for \mathbf{u}_{m+1}^w and \mathbf{v}_{m+1}^w using the backward Euler method for temporal discretization.
3. Update the prestress tensor as $\sigma_{0,(m+1)} = \sigma^s(\mathbf{u}_{m+1}^w) + \sigma_{0,(m)}$.
4. Let tolp denote a prescribed tolerance. If the stopping criterion $\|\mathbf{u}_{m+1}^w\|_{l_2} \leq \text{tolp}$ is satisfied, then set $\sigma_0 = \sigma_{0,(m+1)}$ and exit the fixed-point iteration.

Remark 13. *To minimize cardiac motion artifacts, cardiac images are commonly acquired at diastole via electrocardiogram gating. The fluid boundary traction \mathbf{h}^f at diastole can then be obtained from a separate rigid-wall CFD simulation prescribed with a steady diastolic inflow rate and outlet resistances tuned to achieve the corresponding diastolic pressures and flow splits.*

5.3. Coupling with reduced models

As alluded to in Section 3, zero-dimensional models representing the downstream vasculature are frequently coupled to outlets of the three-dimensional domain [79, 102, 103]. While we restrict our attention to Neumann coupling with zero-dimensional models in which the boundary traction is a function of the flow rate at the corresponding outlet surface only, we note that more generally, any arbitrary combination of Neumann (Dirichlet-to-Neumann) and Dirichlet (Neumann-to-Dirichlet) inlets and outlets and their corresponding system of (nonlinear) ordinary differential equations can be considered [104]. We consider the Neumann boundary Γ_h^f to consist of n_{out} non-overlapping planar outlet surfaces,

$$\Gamma_h^f = \bigcup_{i=1}^{n_{\text{out}}} \Gamma_{\text{out},i}^f, \quad \overline{\Gamma_{\text{out},i}^f} \cap \overline{\Gamma_{\text{out},j}^f} = \emptyset, \text{ for } 1 \leq i, j \leq n_{\text{out}} \text{ and } i \neq j.$$

Let \mathcal{F}^k be a functional operator and $Q^k(t)$ be the volumetric flow rate through the outlet surface $\Gamma_{\text{out},k}^f$,

$$Q^k(t) := \int_{\Gamma_{\text{out},k}^f} \mathbf{v}^f(t) \cdot \mathbf{n} d\Gamma.$$

The boundary traction on $\Gamma_{\text{out},k}^f$ is then given by $\mathbf{h}^f = -P^k(t)\mathbf{n}$, where $P^k(t) = \mathcal{F}^k(Q^k(t))$, and the term (2.27) can be written explicitly as

$$\mathbf{B}_m^h(\mathbf{w}_h^f; \dot{\mathbf{y}}_h^f, \mathbf{y}_h^f) := - \int_{\Gamma_h^f} \mathbf{w}_h^f \cdot \mathbf{h}^f d\Gamma = \sum_{k=1}^{n_{\text{out}}} \mathcal{F}^k(Q^k(t)) \int_{\Gamma_{\text{out},k}^f} \mathbf{w}_h^f \cdot \mathbf{n} d\Gamma.$$

The corresponding contribution to the block matrix $\mathbf{A}_{(l)}$ in (2.55) is then a weighted sum of rank-one matrices. Readers are referred to [51, Section 2.4] for more details of the consistent tangent matrix. The three-element Windkessel model and coronary model, two commonly used zero-dimensional models for Neumann coupling in cardiovascular simulations, are reviewed in Appendix A.

6. Clinical applications

In this section, we apply our combined FSI technology and practical modeling techniques to two patient-specific models, one of the pulmonary arteries of a healthy 9-year-old male and the other of the coronary arteries of a healthy 24-year-old male. Linear tetrahedral meshes were generated with three boundary layers each, at a thickness gradation ratio of 0.5. Patient-specific inflow waveforms were prescribed with parabolic velocity profiles. Outlet boundary conditions were tuned to achieve target inlet systolic and diastolic pressures as well as assumed flow splits (Table 1). Specifically, in the pulmonary model, all outlets were coupled to RCR models, and flow was assumed to be evenly distributed to the left and right lungs; in the coronary model, the aortic outlet was coupled to an RCR model while all remaining outlets were coupled to coronary models. Furthermore, 4% of the flow was distributed to the coronary arteries, with a 60%-40% split for the left and right coronary arteries. Consistent with Section 4.2, we adopt the centimeter-gram-second units, and we set the fluid density ρ^f to 1.0, fluid viscosity μ^f to 0.04, and wall density ρ^s to 1.0. Unless otherwise specified, we set the wall Poisson's ratio ν to 0.5, and the Young's modulus E to 1.3×10^6 uniformly for the pulmonary arteries [105], 7.0×10^6 for the aortic root, and 1.15×10^7 for the coronary arteries [106]. The time step size was chosen to be $T_p/2000$. As discussed in Remark 13, we generated initial conditions for each FSI simulation by first running a rigid-wall CFD simulation to generate solution fields at the diastolic pressure. The prestress generation algorithm was subsequently used to obtain

Model	Sex	Age (year)	R_{in} (cm)	P_{in} (mm Hg)	CO (L/min)	Flow Split	T_p (s)	Outlets
Pulmonary Arteries	M	9	1.24	24 / 8	4.59	50% LPA 50% RPA	0.811	46 RCR
Coronary Arteries	M	24	1.40	123 / 81	3.78	96% AO 2.4% LCOR 1.6% RCOR	1.43	1 RCR 25 coronary

Table 1: Model characteristics. R_{in} : inlet radius; P_{in} : target inlet pressure; CO: prescribed cardiac output; T_p : cardiac period; LPA: left pulmonary artery; RPA: right pulmonary artery; AO: aorta; LCOR: left coronary artery; RCOR: right coronary artery.

the prestress σ_0 balancing the diastolic fluid boundary traction under zero wall displacement relative to the imaged configuration.

All results reported in this section were obtained using the TaiYi supercomputer, a Lenovo system equipped with Intel Xeon Gold 6148 processors interconnected by a 100 GB/s Intel Omni-Path network. Each processor consists of 40 CPUs and 192 GB RAM and operates at a clock rate of 2.4GHz [107].

6.1. Linear solver robustness

We examined the linear solver performance under varying wall properties. For this test, we set the relative tolerance $\delta = 10^{-8}$ for the stopping criterion, and the maximum number of iterations for the outer, intermediate, and inner solvers $n^{\text{max}} = n_{\text{A}}^{\text{max}} = n_{\text{S}}^{\text{max}} = 200$. Relative tolerances δ_{A} and δ_{S} were jointly varied from 10^{-6} to 10^{-2} , and $\delta_{\text{I}} = \sqrt{\delta_{\text{A}}}$. As described in Section 3, the preconditioners \mathbf{P}_{A} and \mathbf{P}_{S} were formed by BoomerAMG based on \mathbf{A} and $\hat{\mathbf{S}}$, respectively.

We additionally compared three other linear solver options. In the first alternative, we applied the block preconditioner without invoking the inner solver, that is, replacing (3.5) in Algorithm 1 with $\hat{\mathbf{S}}\mathbf{y}_p = \mathbf{s}_p$. In the second alternative, we applied the additive Schwarz method to \mathcal{A} , using the incomplete LU factorization for the subdomain solver. In the third alternative, we applied the Jacobi preconditioner to \mathcal{A} . For the latter two alternatives, we increased $n^{\text{max}} = n_{\text{A}}^{\text{max}} = n_{\text{S}}^{\text{max}}$ to 1×10^4 , as significantly more iterations are generally required for convergence.

The pulmonary arterial mesh consists of 2.11×10^6 linear tetrahedral elements and 3.97×10^5 nodes, corresponding to 1.59×10^6 degrees of freedom in the associated linear system. Solver performance was investigated with varying values of the prescribed Young’s modulus over three orders of magnitude, namely $E = 1.3 \times 10^5$, 1.3×10^6 , and 1.3×10^7 . The rigid-wall CFD simulation was also included as the extreme case of an infinitely large Young’s modulus. Simulations were performed on a single node with 16 CPUs. Figure 7 depicts all convergence histories and further annotates the CPU time for the linear solver averaged over ten time steps. We observe that with increasing Young’s moduli, all preconditioners require increasingly more iterations and time to converge. This can be understood from the wall contribution $\mathbf{K}_{\text{m},(l),\hat{\mathbf{u}}^w}$ in (2.55)₁, in which an increased wall stiffness engenders stronger heterogeneity for the block matrix \mathbf{A} . In contrast, no wall contribution is present in the rigid-wall case, and all block preconditioners require fewer iterations and less time to converge. In addition, the additive Schwarz and Jacobi preconditioners closely resemble each other in convergence behavior and are evidently less robust than the block preconditioners, signifying the importance of leveraging the block structure of \mathcal{A} .

The coronary arterial mesh consists of 1.66×10^6 elements and 3.15×10^5 nodes, corresponding to 1.26×10^6 degrees of freedom in the associated linear system. Solver performance was investigated for two values of the Poisson’s ratio $\nu = 0.5$ and 0.3 . Simulations were performed on a single processor with 48 CPUs. Figure 8 depicts all convergence histories and again annotates the CPU time for the linear solver averaged over ten time steps. Only minor differences are observed between the two cases, suggesting a smaller impact of ν on the linear system as compared to E .

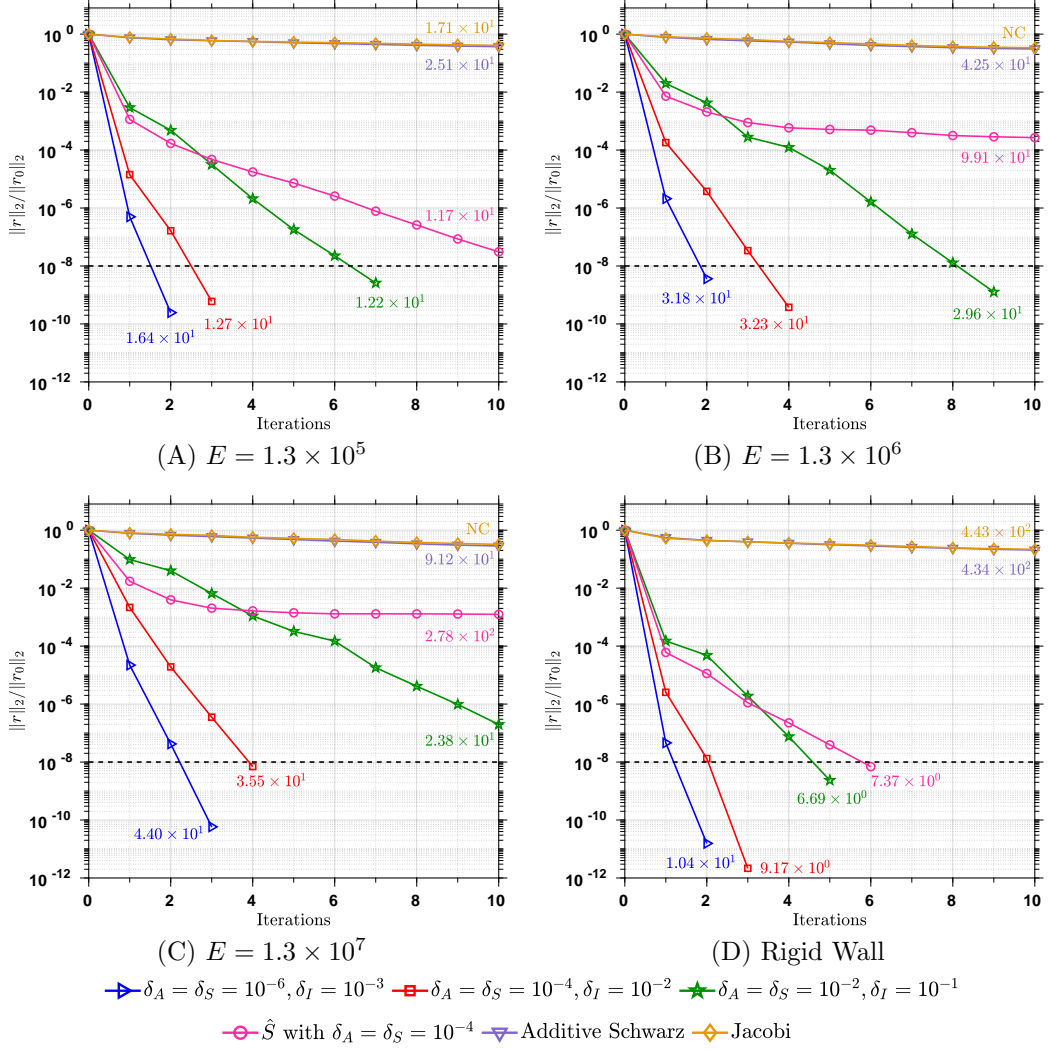


Figure 7: Convergence history for the pulmonary arterial model with varying values of the prescribed Young's modulus. A rigid-wall CFD simulation is also included for comparison. The latter three items in the legend correspond to the three alternative linear solver options investigated. The horizontal dashed black line demarcates the prescribed stopping criterion for the relative error $\delta = 10^{-8}$. CPU times (s) for the linear solver averaged over ten time steps are annotated. NC: no convergence within the prescribed maximum number of iterations.

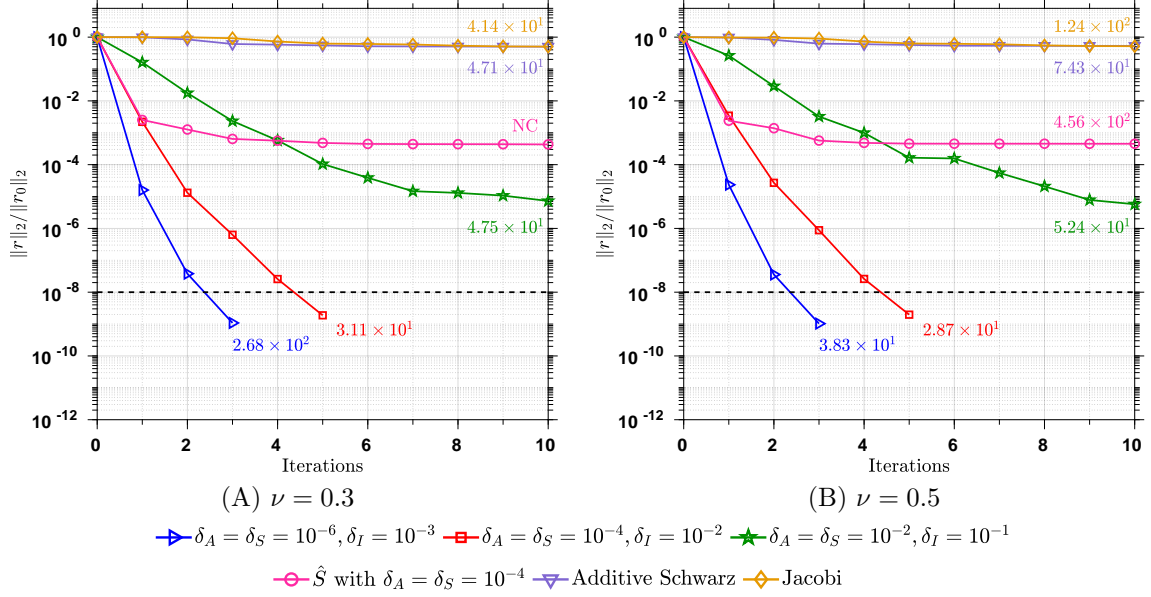


Figure 8: Convergence history for the coronary arterial model with two different values of the Poisson's ratio. The latter three items in the legend correspond to the three alternative linear solver options investigated. The horizontal dashed black line demarcates the prescribed stopping criterion for the relative error $\delta = 10^{-8}$. CPU times (s) for the linear solver averaged over ten time steps are annotated. NC: no convergence within the prescribed maximum number of iterations.

6.2. Fixed-size scalability

We examined the parallel performance of our proposed solution strategy, setting the relative tolerances $\delta = 10^{-8}$, $\delta_A = \delta_S = 10^{-4}$, and $\delta_I = 10^{-2}$. While the same pulmonary arterial mesh was used as in Section 6.1, we used a finer coronary mesh of 6.44×10^6 linear elements and 1.25×10^6 nodes, corresponding to 5.01×10^6 degrees of freedom in the associated linear system. Speed-up ratios were calculated based on a serial simulation for the pulmonary mesh and a parallel simulation with 20 CPUs for the coronary mesh. Each job was run for 20 time steps. For the pulmonary arterial mesh, super-optimal parallel efficiency was observed for 2 and 4 CPUs (Figure 9), likely a consequence of more efficient utilization of the cache in these scenarios.

6.3. Performance of the segregated predictor multi-corrector algorithm

As discussed above in Remark 9, we have conveniently chosen $\mathbf{R}_{k,(l)} = \mathbf{0}$ for all $l \geq 1$ to allow for the simplified right-hand side in the linear system (2.56) in the segregated predictor multi-corrector algorithm. In Table 2, we document the nonlinear residual $\mathbf{R}_{(l)}$ and kinematic residual $\mathbf{R}_{k,(l)}$ at all Newton-Raphson iterations within two time steps of the cardiac cycle for each model, one at peak systole and the other at mid-diastole. We note that $\mathbf{R}_{k,(l)} < 10^{-12}$ beginning with $l = 1$ and is driven close to machine precision for $l \geq 2$, closely agreeing with our prior analysis of the segregated algorithm [81]. We also note the expected quadratic convergence of the relative nonlinear residual in the first two iterations of the Newton-Raphson procedure. The convergence rate from the second to the third iteration is slightly reduced, likely a consequence of the linear solver accuracy.

6.4. Simulation with higher-order elements

Given limitations of the meshing software MeshSim, we were unable to generate a suite of spatially homogeneous quadratic tetrahedral meshes with boundary layers that would be of tractable computational cost. We therefore investigated the spatial convergence of peak systolic WSS with isotropic pulmonary

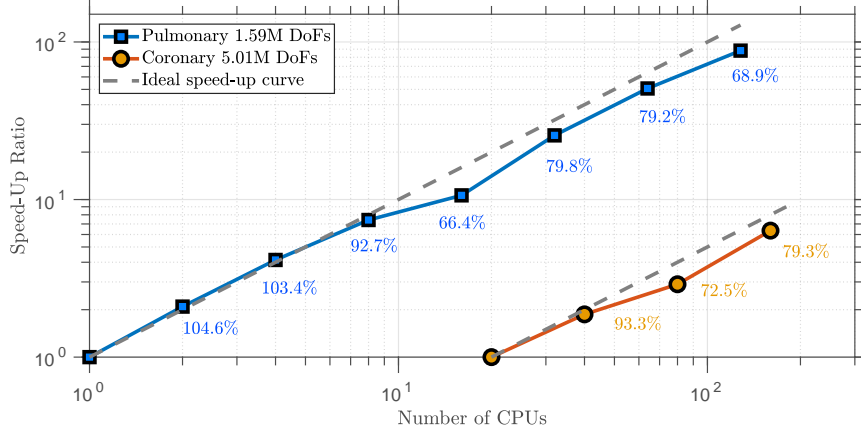


Figure 9: Fixed-size scalability of our solution strategy. Annotated efficiency rates are computed from the total runtime.

Model	n	l	$\mathbf{R}_{(l)}/\mathbf{R}_{(0)}$	$\mathbf{R}_{k,(l)}$
Pulmonary	491	1	3.40×10^{-1}	4.73×10^{-15}
		2	1.81×10^{-5}	4.51×10^{-16}
		3	1.09×10^{-7}	6.78×10^{-21}
	1246	1	2.23×10^{-1}	3.08×10^{-15}
		2	3.71×10^{-5}	2.35×10^{-16}
		3	1.08×10^{-7}	3.50×10^{-18}
Coronary	446	1	2.64×10^0	2.49×10^{-13}
		2	4.22×10^{-4}	4.93×10^{-14}
		3	2.78×10^{-7}	4.44×10^{-16}
	1223	1	2.28×10^0	6.45×10^{-14}
		2	8.51×10^{-5}	1.18×10^{-14}
		3	4.12×10^{-8}	1.94×10^{-18}

Table 2: The nonlinear residual $\mathbf{R}_{(l)}$ and kinematic residual $\mathbf{R}_{k,(l)}$ at all nonlinear iterations within time steps corresponding to peak systole and mid-diastole.

arterial meshes of linear and quadratic tetrahedral elements at three refinement levels of comparable numbers of nodes (4.0×10^5 , 8.0×10^5 , and 1.6×10^6 nodes). For each model, the coarsest isotropic mesh was chosen to match the number of nodes in the linear tetrahedral mesh with three boundary layers used in Section 6.1. WSS results from the boundary layer mesh were verified to be mesh independent and taken as reference values. Consistent with observations from our spatial convergence study in Section 4.1, quadratic elements resolve WSS more accurately (Figure 10). We do, however, note the presence of undesirable oscillations yielding sharp local gradients and local WSS over/underestimations.

6.5. Patient-specific simulations

In order to assess our proposed techniques for variable wall thickness assignment and tissue prestressing, three simulations were performed for each model: (i) an unprestressed simulation with centerline-based thickness, (ii) a prestressed simulation with centerline-based thickness, (iii) a prestressed simulation with Laplacian-based thickness. In the centerline-based approach, the local thickness was prescribed to be 20% of the local radius everywhere; in the Laplacian approach, the thickness was prescribed to be 20% of the corresponding cap radius at all wall boundary nodes (Figure 11A). Simulations were performed over three cardiac cycles with uniform time steps and verified for convergence to a limit cycle. For each simulation, only the final cardiac cycle was analyzed.

The wall displacement and WSS distributions at peak systole were compared across the three cases (Figure 11B). Relative to Simulation (ii), failure to consider tissue prestressing in Simulation (i) *overestimates* the maximum wall displacement magnitude by 37.9% (0.189 vs. 0.137 cm) in the pulmonary arterial model and by 162% (0.119 vs. 0.0453 cm) in the coronary arterial model. It also overestimates the mean displacement magnitude by 29.4% (0.0616 vs. 0.0476 cm) over the main pulmonary arterial (MPA) bifurcation, by 159% (0.01829 vs. 0.00707 cm) over the aortic root, and by 183% (0.0267 vs. 0.00942 cm) over the left coronary artery (LCOR). While prestressing yields significantly different displacements in both models, our results suggest that prestressing is particularly critical in the systemic circulation where the diastolic pressure is an order of magnitude larger than that in the pulmonary circulation. In contrast, the Laplacian-based thickness in Simulation (iii) *underestimates* the mean displacement magnitude by 29.8% (0.0334 vs. 0.0453 cm) over the MPA bifurcation, by 45.3% (0.00387 vs. 0.00707 cm) over the aortic root, and by 45.7% (0.00511 vs. 0.00942 cm) over the LCOR. We note that while we prescribed Young’s moduli that were previously determined to yield cross-sectional relative area changes observed from PC-MRI, tissue prestressing was not considered in these prior studies [105, 106]. More compliant wall properties would thus need to be considered to achieve the same relative area changes under prestressing.

While local discrepancies in peak systolic WSS are also observed across the three cases (as highlighted by the red arrows in Figure 11(B)), these drastic discrepancies in displacement do not produce discrepancies in volumetric flow rates or spatially averaged WSS quantities. In fact, the mean WSS magnitude only differs by up to 2.03% over the MPA bifurcation, 0.174% over the aorta, and 0.149% over the LCOR. Despite the rationale behind our proposed modeling techniques, the merits of Simulation (ii) remain to be assessed with in vivo and/or in vitro validation data.

7. Conclusions

In this work, we derived a reduced unified continuum formulation for vascular FSI and presented strong verification of our numerical methodology against Womersley’s deformable wall theory using both linear and quadratic tetrahedral elements. Compared to the unified continuum ALE formulation, our reduced theory invokes three assumptions for the vascular wall to achieve monolithic FSI coupling in the Eulerian frame for small-strain problems. The residual-based VMS formulation is adopted for spatial discretization, and the generalized- α method is adopted for temporal discretization such that velocity and pressure are uniformly second-order accurate in time, a significant improvement over the predominant dichotomous approach. Block preconditioning of a monolithically coupled FSI system is also performed for the first time. Using two patient-specific models, we demonstrated the fixed-size scalability and enhanced robustness of our nested block preconditioner as compared to alternative preconditioners for vascular FSI applications.

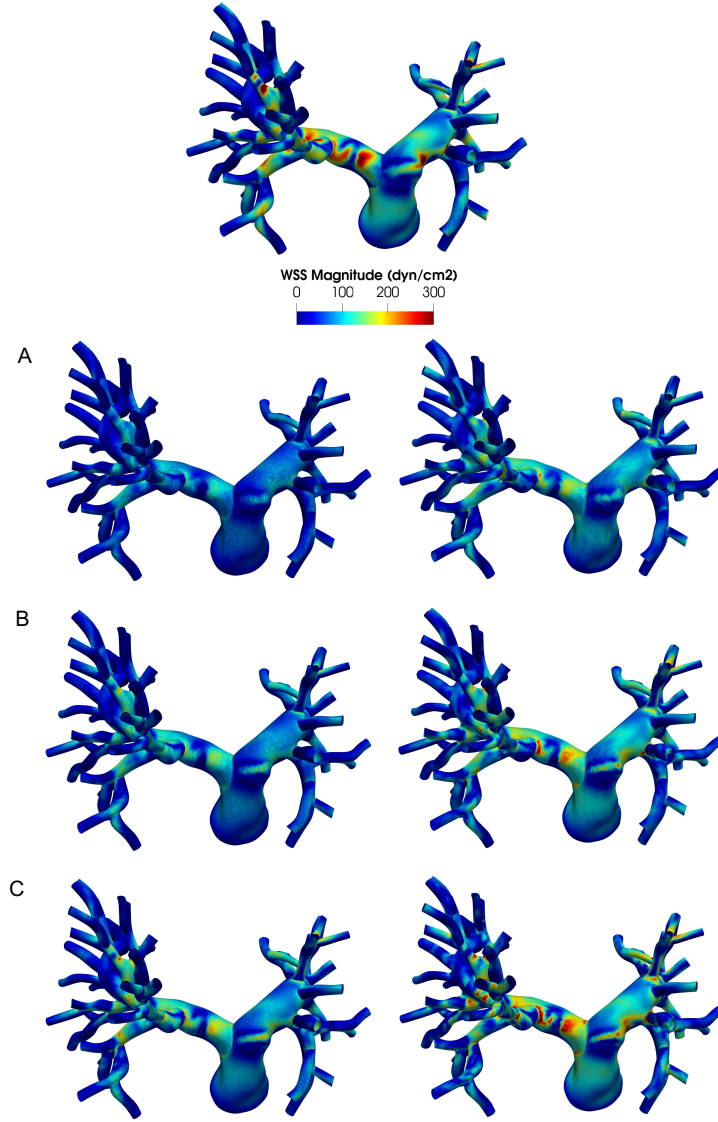


Figure 10: Spatial convergence of peak systolic WSS using isotropic linear (left) and quadratic (right) tetrahedral meshes of the pulmonary arterial model at three refinement levels: (A) 4.0×10^5 nodes, (B) 8.0×10^5 nodes, (C) 1.6×10^6 nodes.

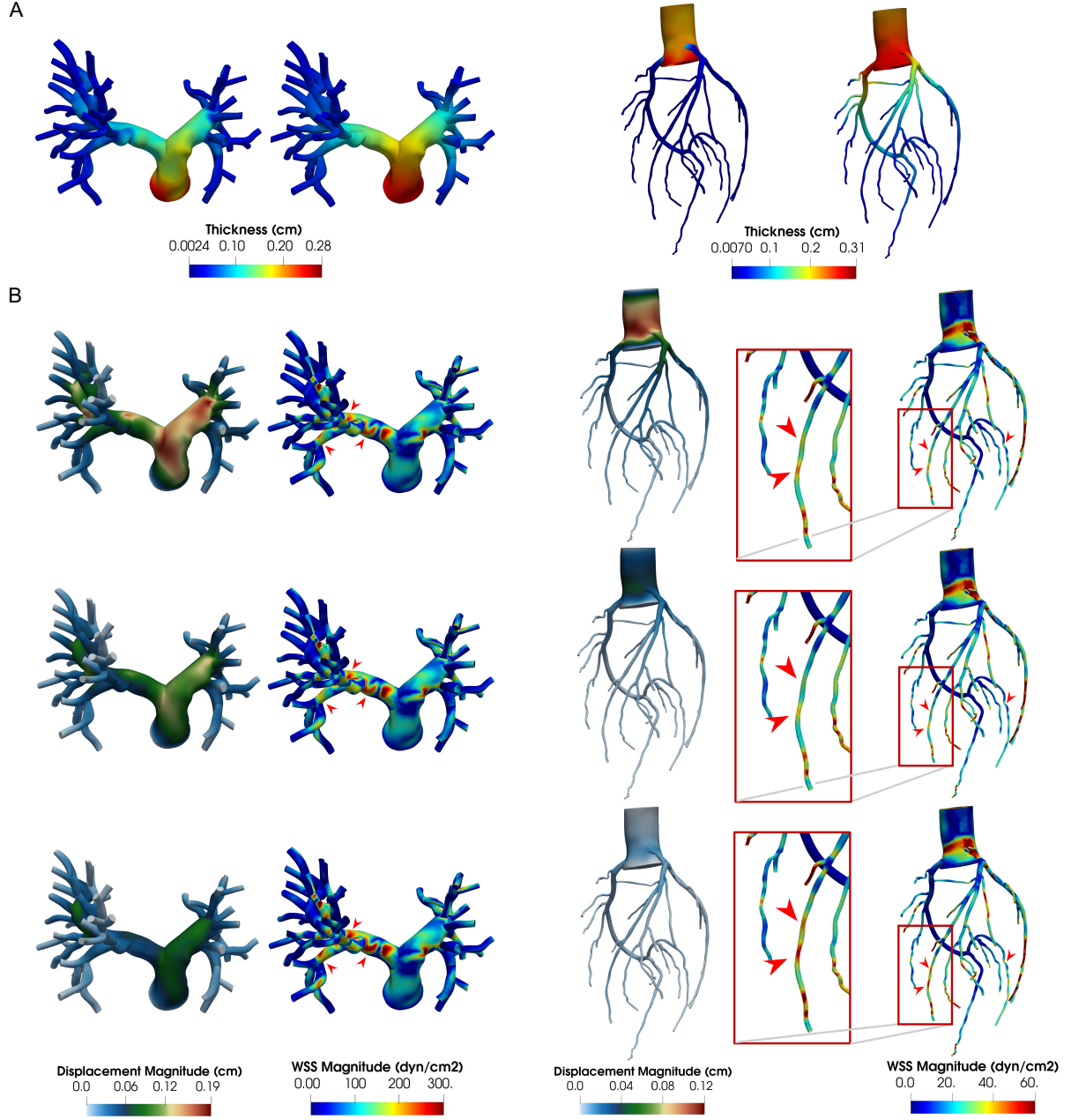


Figure 11: Effects of different wall thickness distributions and tissue prestressing on patient-specific pulmonary (left) and coronary (right) arterial models. (A) Centerline-based (left) and Laplacian wall thickness distributions. (B) Peak systolic wall displacement (left) and wall shear stress (WSS; right) magnitudes for unprestressed simulations with centerline-based thickness (top), prestressed simulations with centerline-based thickness (middle), and prestressed simulations with Laplacian-based thickness (bottom). Red arrows and detailed views are included to highlight WSS differences across the three cases.

To appropriately model physiological phenomena, we further outlined a centerline-based approach for wall thickness assignment and a fixed-point algorithm for prestressing the vascular wall at the imaged configuration. Validation of our combined FSI methodology against in vivo and/or in vitro data will be examined in future studies.

Acknowledgements

This work was supported by the National Institutes of Health [grant numbers 1R01HL121754, 1R01HL123689, R01EB01830204], Southern University of Science and Technology [startup grant number Y01326127], the National Natural Science Foundation of China [grant number 12172160], and the Guangdong-Hong Kong-Macao Joint Laboratory for Data-Driven Fluid Mechanics and Engineering Applications [grant number 2020B1212030001]. Ingrid S. Lan was supported by the National Science Foundation (NSF) Graduate Research Fellowship and the Stanford Graduate Fellowship in Science and Engineering. Computational resources were provided by the Stanford Research Computing Center, the Extreme Science and Engineering Discovery Environment supported by NSF [grant number ACI-1053575], and the Center for Computational Science and Engineering at Southern University of Science and Technology.

References

- [1] C. Hirt, A. Amsden, J. Cook, An arbitrary Lagrangian-Eulerian computing method for all flow speeds, *Journal of Computational Physics* 14 (1974) 227–253.
- [2] T. Hughes, W. Liu, T. Zimmermann, Lagrangian-Eulerian finite element formulation for incompressible viscous flows, *Computer Methods in Applied Mechanics and Engineering* 29 (1981) 329–349.
- [3] J. Donea, S. Giuliani, J. Halleux, An arbitrary Lagrangian-Eulerian finite-element method for transient dynamic fluid structure interactions, *Computer Methods in Applied Mechanics and Engineering* 33 (1982) 689–723.
- [4] C. Peskin, Flow patterns around heart valves: A numerical method, *Journal of Computational Physics* 10 (1972) 252–271.
- [5] R. Mittal, G. Iaccarino, Immersed boundary methods, *Annual Review of Fluid Mechanics* 37 (2005) 239–261.
- [6] F. Baaijens, A fictitious domain/mortar element method for fluid-structure interaction, *International Journal for Numerical Methods in Fluids* 35 (2001) 743–761.
- [7] I. Borazjani, Fluid-structure interaction, immersed boundary-finite element method simulations of bio-prosthetic heart valves, *Computer Methods in Applied Mechanics and Engineering* 257 (2013) 103–116.
- [8] B. Griffith, X. Luo, D. McQueen, C. Peskin, Simulating the fluid dynamics of natural and prosthetic heart valves using the immersed boundary method, *International Journal of Applied Mechanics* 1 (2009) 137–177.
- [9] D. Kamensky, M. Hsu, D. Schillinger, J. Evans, A. Aggarwal, Y. Bazilevs, M. Sacks, T. Hughes, An immersogeometric variational framework for fluid-structure interaction: Application to bioprosthetic heart valves, *Computer Methods in Applied Mechanics and Engineering* 284 (2015) 1005–1053.
- [10] J. de Hart, G. Peters, P. Schreurs, F. Baaijens, A three-dimensional computational analysis of fluid-structure interaction in the aortic valve, *Journal of Biomechanics* 36 (2003) 103–112.
- [11] R. van Loon, P. Anderson, F. van de Vosse, A fluid-structure interaction method with solid-rigid contact for heart valve dynamics, *Journal of Computational Physics* 217 (2006) 806–823.
- [12] Y. Wu, X. Cai, A fully implicit domain decomposition based ALE framework for three-dimensional fluid-structure interaction with application in blood flow computation, *Journal of Computational Physics* 258 (2014) 524–537.
- [13] M. Hsu, D. Kamensky, Y. Bazilevs, M. Sacks, T. Hughes, Fluid-structure interaction analysis of bioprosthetic heart valves: significance of arterial wall deformation, *Computational Mechanics* 54 (2014) 1055–1071.
- [14] J. Liu, A. Marsden, A unified continuum and variational multiscale formulation for fluids, solids, and fluid-structure interaction, *Computer Methods in Applied Mechanics and Engineering* 337 (2018) 549–597.
- [15] J. Liu, W. Yang, I. Lan, A. Marsden, Fluid-structure interaction modeling of blood flow in the pulmonary arteries using the unified continuum and variational multiscale formulation, *Mechanics Research Communications* 107 (2020) 103556.
- [16] M. Fernández, Coupling schemes for incompressible fluid-structure interaction: implicit, semi-implicit and explicit, *SeMA Journal* 55 (2011) 59–108.
- [17] F. Nobile, M. Pozzoli, C. Vergara, Time accurate partitioned algorithms for the solution of fluid-structure interaction problems in haemodynamics, *Computers & Fluids* 86 (2013) 470–482.
- [18] S. Piperno, C. Farhat, Design of Efficient Partitioned Procedures for the Transient Solution of Aeroelastic Problems, *European Journal of Computational Mechanics* 9 (2000) 655–680.
- [19] S. Badia, A. Quaini, A. Quarteroni, Modular vs. non-modular preconditioners for fluid-structure systems with large added-mass effect, *Computer Methods in Applied Mechanics and Engineering* 197 (2008) 4216–4232.
- [20] P. Causin, J. Gerbeau, F. Nobile, Added-mass effect in the design of partitioned algorithms for fluid-structure problems, *Computer Methods in Applied Mechanics and Engineering* 194 (2005) 4506–4527.
- [21] G. Guidoboni, R. Glowinski, N. Cavallini, S. Canic, Stable loosely-coupled-type algorithm for fluid-structure interaction in blood flow, *Journal of Computational Physics* 228 (2009) 6916–6937.

- [22] S. Badia, F. Nobile, C. Vergara, Fluid-structure partitioned procedures based on Robin transmission conditions, *Journal of Computational Physics* 227 (2008) 7027–7051.
- [23] C. Kadapa, Insights into the performance of loosely-coupled FSI schemes based on Robin boundary conditions, *arXiv preprint arXiv:2105.14831* (2021).
- [24] C. Figueroa, I. Vignon-Clementel, K. Jansen, T. Hughes, C. Taylor, A coupled momentum method for modeling blood flow in three-dimensional deformable arteries, *Computer Methods in Applied Mechanics and Engineering* 195 (2006) 5685–5706.
- [25] N. Nama, M. Aguirre, J. Humphrey, C. Figueroa, A nonlinear rotation-free shell formulation with prestressing for vascular biomechanics, *Scientific Reports* 10 (2020) 17528.
- [26] J. Womersley, Oscillatory motion of a viscous liquid in a thin-walled elastic tube—I: The linear approximation for long waves, *The London, Edinburgh, and Dublin Philosophical Magazine and Journal of Science* 46 (1955) 199–221.
- [27] M. Zamir, *The physics of pulsatile flow*, Springer, New York, 2000.
- [28] A. Updegrove, N. Wilson, J. Merkow, H. Lan, A. Marsden, S. Shadden, SimVascular: An Open Source Pipeline for Cardiovascular Simulation, *Annals of Biomedical Engineering* 45 (2017) 525–541.
- [29] H. Lan, A. Updegrove, N. M. Wilson, G. D. Maher, S. C. Shadden, A. L. Marsden, A Re-Engineered Software Interface and Workflow for the Open-Source SimVascular Cardiovascular Modeling Package, *Journal of Biomechanical Engineering* 140 (2) (2018) 0245011–02450111.
- [30] C. Arthurs, R. Khlebnikov, A. Melville, A. Gomez, D. Dillon-Murphy, F. Cuomo, M. Vieira, J. Schollenberger, S. Lynch, C. Tossas-Betancourt, et al., Crimson: An open-source software framework for cardiovascular integrated modelling and simulation, *bioRxiv* (2020).
- [31] A. Williams, B. Koo, T. Gundert, P. Fitzgerald, J. L. Jr., Local hemodynamic changes caused by main branch stent implantation and subsequent virtual side branch balloon angioplasty in a representative coronary bifurcation, *Journal of Applied Physiology* 109 (2010) 532–540.
- [32] T. Gundert, S. Shadden, A. Williams, B. Koo, J. Feinstein, J. L. Jr., A rapid and computationally inexpensive method to virtually implant current and next-generation stents into subject-specific computational fluid dynamics models, *Annals of Biomedical Engineering* 39 (2011) 1423–1437.
- [33] C. Taylor, T. Fonte, J. Min, Computational Fluid Dynamics Applied to Cardiac Computed Tomography for Noninvasive Quantification of Fractional Flow Reserve: Scientific Basis, *Journal of the American College of Cardiology* 61 (2013) 2233–2241.
- [34] J. Coogan, F. Chan, C. Taylor, J. Feinstein, Computational fluid dynamic simulations of aortic coarctation comparing the effects of surgical- and stent-based treatments on aortic compliance and ventricular workload, *Catheterization and Cardiovascular Interventions* 77 (2010) 680–691.
- [35] W. Yang, J. Feinstein, A. Marsden, Constrained optimization of an idealized Y-shaped baffle for the Fontan surgery at rest and exercise, *Computer Methods in Applied Mechanics and Engineering* 199 (2010) 2135–2149.
- [36] W. Yang, J. Feinstein, I. Vignon-Clementel, Adaptive outflow boundary conditions improve post-operative predictions after repair of peripheral pulmonary artery stenosis, *Biomechanics and Modeling in Mechanobiology* 15 (2016) 1345–1353.
- [37] W. Yang, F. Hanley, F. Chan, A. Marsden, I. Vignon-Clementel, J. Feinstein, Computational simulation of postoperative pulmonary flow distribution in Alagille patients with peripheral pulmonary artery stenosis, *Congenital Heart Disease* 13 (2017) 241–250.
- [38] E. Kung, A. Les, C. Figueroa, F. Medina, K. Arcaute, R. Wicker, M. McConnell, C. Taylor, In vitro validation of finite element analysis of blood flow in deformable models, *Annals of Biomedical Engineering* 39 (2011) 1947–1960.
- [39] E. Kung, A. Les, F. Medina, R. Wicker, M. McConnell, C. Taylor, In vitro validation of finite-element model of AAA hemodynamics incorporating realistic outlet boundary conditions, *Journal of Biomechanical Engineering* (2011).
- [40] C. Figueroa, A Coupled-Momentum Method to Model Blood Flow and Vessel Deformation in Human Arteries: Applications in Disease Research and Simulation-Based Medical Planning, Ph.D. thesis, Stanford University (2006).
- [41] V. Filonova, C. Arthurs, I. Vignon-Clementel, C. Figueroa, Verification of the coupled-momentum method with Womersley’s Deformable Wall analytical solution, *International Journal for Numerical Methods in Biomedical Engineering* 36 (2019) e3266.
- [42] Y. Bazilevs, V. Calo, J. Cottrell, T. Hughes, A. Reali, G. Scovazzi, Variational multiscale residual-based turbulence modeling for large eddy simulation of incompressible flows, *Computer Methods in Applied Mechanics and Engineering* 197 (2007) 173–201.
- [43] J. Chung, G. Hulbert, A Time Integration Algorithm for Structural Dynamics With Improved Numerical Dissipation: The Generalized- α Method, *Journal of Applied Mechanics* 60 (1993) 371–375.
- [44] K. Jansen, C. Whiting, G. Hulbert, A generalized- α method for integrating the filtered Navier-Stokes equations with a stabilized finite element method, *Computer Methods in Applied Mechanics and Engineering* 190 (2000) 305–319.
- [45] Y. Bazilevs, V. Calo, T. Hughes, Y. Zhang, Isogeometric fluid-structure interaction: theory, algorithms, and computations, *Computational Mechanics* 43 (2008) 3–37.
- [46] Y. Bazilevs, K. Takizawa, T. Tezduyar, *Computational Fluid-Structure Interaction: Methods and Applications*, John Wiley & Sons, Ltd, 2012.
- [47] V. Joshi, R. Jaiman, A hybrid variational Allen-Cahn/ALE scheme for the coupled analysis of two-phase fluid-structure interaction, *International Journal for Numerical Methods in Engineering* 117 (2018) 405–429.
- [48] S. Kang, H. Choi, J. Yoo, Investigation of fluid-structure interactions using a velocity-linked P2/P1 finite element method and the generalized- α method, *International Journal for Numerical Methods in Engineering* 90 (2012) 1529–1548.
- [49] J. Liu, I. Lan, O. Tikenogullari, A. Marsden, A note on the accuracy of the generalized- α scheme for the incompressible Navier-Stokes equations, *International Journal for Numerical Methods in Engineering* 122 (2021) 638–651.

- [50] N. Newmark, A method of computation for structural dynamics, *Proceedings of the American Society of Civil Engineers: Journal of the Engineering Mechanics Division* (1959) 67–94.
- [51] J. Liu, W. Yang, M. Dong, A. Marsden, The nested block preconditioning technique for the incompressible Navier-Stokes equations with emphasis on hemodynamic simulations, *Computer Methods in Applied Mechanics and Engineering* 367 (2020) 113122.
- [52] T. Hughes, *The Finite Element Method: Linear Static and Dynamic Finite Element Analysis*, Prentice-Hall, 1987.
- [53] J. Liu, A. Marsden, Z. Tao, An energy-stable mixed formulation for isogeometric analysis of incompressible hyperelastodynamics, *International Journal for Numerical Methods in Engineering* 120 (2019) 937–963.
- [54] C. Colciago, S. DeParis, A. Quarteroni, Comparisons between reduced order models and full 3D models for fluid-structure interaction problems in haemodynamics, *Journal of Computational and Applied Mathematics* 265 (2014) 120–138.
- [55] G. Hulbert, *Encyclopedia of Computational Mechanics*, John Wiley & Sons, Ltd, 2017, Ch. Computational Structural Dynamics.
- [56] J. Alastruey, K. Parker, S. Sherwin, 11th International Conference on Pressure Surges, Virtual PiE Led t/a BHR Group, 2012, Ch. Arterial pulse wave haemodynamics, pp. 401–443.
- [57] Y. Bazilevs, M. Hsu, D. Benson, S. Sankaran, A. Marsden, Computational fluid-structure interaction: methods and application to a total cavopulmonary connection, *Computational Mechanics* 45 (2009) 77–89.
- [58] M. Bischoff, K.-U. Bletzinger, W. Wall, E. Ramm, *Encyclopedia of Computational Mechanics*, John Wiley & Sons, Ltd., 2004, Ch. Models and Finite Elements for Thin-Walled Structures, pp. 59–137.
- [59] P. Bergan, C. Felippa, A triangular membrane element with rotational degrees of freedom, *Computer Methods in Applied Mechanics and Engineering* 50 (1985) 25–69.
- [60] H. Jun, K. Yoon, P. Lee, K. Bathe, The MITC3+ shell element enriched in membrane displacements by interpolation covers, *Computer Methods in Applied Mechanics and Engineering* 337 (2018) 458–480.
- [61] J. Debes, Y. Fung, Biaxial mechanics of excised canine pulmonary arteries, *American Journal of Physiology* 269 (1995) H433–H442.
- [62] J. Zhou, Y. Fung, The degree of nonlinearity and anisotropy of blood vessel elasticity, *Proceedings of the National Academy of Sciences of the United States of America* 94 (1997) 14255–14260.
- [63] L. Franca, S. Frey, Stabilized finite element methods: II. The incompressible Navier-Stokes equations, *Computer Methods in Applied Mechanics and Engineering* 99 (1992) 209–233.
- [64] Y. Bazilevs, J. Gohean, T. Hughes, R. Moser, Y. Zhang, Patient-specific isogeometric fluid-structure interaction analysis of thoracic aortic blood flow due to implantation of the Jarvik 2000 left ventricular assist device, *Computer Methods in Applied Mechanics and Engineering* 198 (2009) 3534–3550.
- [65] M. Moghadam, Y. Bazilevs, T. Hsia, I. Vignon-Clementel, A. Marsden, Modeling Of Congenital Hearts Alliance (MOCHA), A comparison of outlet boundary treatments for prevention of backflow divergence with relevance to blood flow simulations, *Computational Mechanics* 48 (2011) 277–291.
- [66] C. Taylor, T. Hughes, C. Zarins, Finite element modeling of blood flow in arteries, *Computer Methods in Applied Mechanics and Engineering* 158 (1998) 155–196.
- [67] P. Gresho, R. Sani, *Incompressible flow and the finite element method. Volume 1: Advection-diffusion and isothermal laminar flow*, John Wiley & Sons, Inc., New York, NY (United States), 1998.
- [68] Y. Bazilevs, C. Michler, V. Calo, T. Hughes, Weak Dirichlet boundary conditions for wall-bounded turbulent flows, *Computer Methods in Applied Mechanics and Engineering* 196 (2007) 4853–4862.
- [69] O. Colomés, S. Badia, R. Codina, J. Principe, Assessment of variational multiscale models for the large eddy simulation of turbulent incompressible flows, *Computer Methods in Applied Mechanics and Engineering* 285 (2015) 32–63.
- [70] A. Brooks, T. Hughes, Streamline upwind/Petrov-Galerkin formulations for convection dominated flows with particular emphasis on the incompressible Navier-Stokes equations, *Computer Methods in Applied Mechanics and Engineering* 32 (1982) 199–259.
- [71] T. Hughes, L. Mazzei, K. Jansen, Large eddy simulation and the variational multiscale method, *Computing and Visualization in Science* 3 (2000) 47–59.
- [72] L. Pauli, M. Behr, On stabilized space-time FEM for anisotropic meshes: Incompressible Navier-Stokes equations and applications to blood flow in medical devices, *International Journal for Numerical Methods in Fluids* 85 (2017) 189–209.
- [73] M. von Danwitz, V. Karyofylli, N. Hosters, M. Behr, Simplex space-time meshes in compressible flow simulations, *International Journal for Numerical Methods in Fluids* 91 (2019) 29–48.
- [74] C. Figueroa, C. Taylor, A. Marsden, *Encyclopedia of Computational Mechanics*, John Wiley & Sons, Ltd, 2017, Ch. Blood Flow.
- [75] C. Taylor, C. Figueroa, Patient-specific modeling of cardiovascular mechanics, *Annual Review of Biomedical Engineering* 11 (2009).
- [76] J. Simo, N. Tarnow, K. Wong, Exact energy-momentum conserving algorithms and symmetric schemes for nonlinear dynamics, *Computer Methods in Applied Mechanics and Engineering* 100 (1992) 63–116.
- [77] H. Hilber, T. Hughes, Collocation, dissipation and ‘overshoot’ for time integration schemes in structural dynamics, *Earthquake Engineering & Structural Dynamics* 6 (1978) 99–117.
- [78] C. Kadapa, W. Dettmer, D. Perić, On the advantages of using the first-order generalised-alpha scheme for structural dynamic problems, *Computers & Structures* 193 (2017) 226–238.
- [79] M. Moghadam, I. Vignon-Clementel, R. Figliola, A. Marsden, Modeling Of Congenital Hearts Alliance (MOCHA) Investigators, A modular numerical method for implicit 0D/3D coupling in cardiovascular finite element simulations, *Journal of Computational Physics* 244 (2013) 63–79.
- [80] G. Scovazzi, B. Carnes, X. Zeng, S. Rossi, A simple, stable, and accurate linear tetrahedral finite element for transient,

- nearly, and fully incompressible solid dynamics: a dynamic variational multiscale approach, *International Journal for Numerical Methods in Engineering* 106 (2016) 799–839.
- [81] J. Liu, A. Marsden, A robust and efficient iterative method for hyper-elastodynamics with nested block preconditioning, *Journal of Computational Physics* 383 (2019) 72–93.
 - [82] Z. Johan, T. Hughes, A globally convergent matrix-free algorithm for implicit time-marching schemes arising in finite element analysis in fluids, *Computer Methods in Applied Mechanics and Engineering* 87 (1991) 281–304.
 - [83] M. Benzi, G. Golub, J. Liesen, Numerical solution of saddle point problems, *Acta numerica* 14 (2005) 1–137.
 - [84] D. May, L. Moresi, Preconditioned iterative methods for Stokes flow problems arising in computational geodynamics, *Physics of the Earth and Planetary Interiors* 171 (2008) 33–47.
 - [85] Y. Saad, A flexible inner-outer preconditioned GMRES algorithm, *SIAM Journal on Scientific Computing* 14 (1993) 461–469.
 - [86] A. Ieary, R. Falgout, V. Henson, J. Jones, T. Manteuffel, S. McCormick, G. Miranda, J. Ruge, Robustness and scalability of algebraic multigrid, *SIAM Journal on Scientific Computing* 21 (5) (2000) 1886–1908.
 - [87] P. Wesseling, C. Oosterlee, Geometric multigrid with applications to computational fluid dynamics, *Journal of computational and applied mathematics* 128 (1-2) (2001) 311–334.
 - [88] R. Falgout, U. Yang, hypre: A library of high performance preconditioners, in: *International Conference on Computational Science*, Springer, 2002, pp. 632–641.
 - [89] J. Brown, Efficient nonlinear solvers for nodal high-order finite elements in 3D, *Journal of Scientific Computing* 45 (2010) 48–63.
 - [90] D. Davydov, J. Pelteret, D. Arndt, M. Kronbichler, P. Steinmann, A matrix-free approach for finite-strain hyperelastic problems using geometric multigrid, *International Journal for Numerical Methods in Engineering* 121 (2020) 2874–2895.
 - [91] D. Knoll, D. Keyes, Jacobian-free Newton-Krylov methods: a survey of approaches and applications, *Journal of Computational Physics* 193 (2004) 357–397.
 - [92] svSolver GitHub repository, github.com/SimVascular/svSolver/blob/master/Code/FlowSolvers/ThreeDSolver/svSolver.
 - [93] J. Humphrey, *Cardiovascular Solid Mechanics: Cells, Tissues, and Organs*, Springer Science + Business Media, 2002.
 - [94] J. Wong, E. Kuhl, Generating fibre orientation maps in human heart models using Poisson interpolation, *Computer Methods in Biomechanics and Biomedical Engineering* 17 (11) (2014) 1217–1226.
 - [95] N. Xiao, J. Humphrey, C. Figueroa, Multi-Scale Computational Model of Three-Dimensional Hemodynamics within a Deformable Full-Body Arterial Network, *Journal of Computational Physics* 244 (2013) 22–40.
 - [96] The Vascular Modeling ToolKit, www.vmtk.org.
 - [97] L. Antiga, M. Piccinelli, L. Botti, B. Ene-Iordache, A. Remuzzi, D. Steinman, An image-based modeling framework for patient-specific computational hemodynamics, *Medical & Biological Engineering & Computing* 46 (2008) 1097.
 - [98] L. Antiga, Patient-Specific Modeling of Geometry and Blood Flow in Large Arteries, Ph.D. thesis, Polytechnic University of Milan (2002).
 - [99] T. Tezduyar, S. Sathe, M. Schwaab, B. Conklin, Arterial fluid mechanics modeling with the stabilized space-time fluid–structure interaction technique, *International Journal for Numerical Methods in Fluids* 57 (5) (2008) 601–629.
 - [100] M.-C. Hsu, Y. Bazilevs, Blood vessel tissue prestress modeling for vascular fluid–structure interaction simulation, *Finite Elements in Analysis and Design* 47 (6) (2011) 593–599.
 - [101] K. Bäuml, V. Vedula, A. Sailer, J. Seo, P. Chiu, G. Mistelbauer, F. Chan, M. Fischbein, A. Marsden, D. Fleischmann, Fluid-structure interaction simulations of patient-specific aortic dissection, *Biomechanics and Modeling in Mechanobiology* <https://doi.org/10.1007/s10237-020-01294-8> (2020).
 - [102] I. Vignon-Clementel, C. Figueroa, K. Jansen, C. Taylor, Outflow boundary conditions for three-dimensional finite element modeling of blood flow and pressure in arteries, *Computer Methods in Applied Mechanics and Engineering* 195 (2006) 3776–3796.
 - [103] I. Vignon-Clementel, C. Figueroa, K. Jansen, C. Taylor, Outflow boundary conditions for 3D simulations of non-periodic blood flow and pressure fields in deformable arteries., *Computer Methods in Biomechanics and Biomedical Engineering* 13 (2010) 625–640.
 - [104] E. Kung, C. Corsini, A. Marsden, I. Vignon-Clementel, G. Pennati, R. Figliola, T.-Y. Hsia, Modeling Of Congenital Hearts Alliance (MOCHA) Investigators, Multiscale Modeling of Superior Cavopulmonary Circulation: Hemi-Fontan and Bidirectional Glenn Are Equivalent, *Seminars in Thoracic and Cardiovascular Surgery* 32 (4) (2020) 883–892.
 - [105] W. Yang, M. Dong, M. Rabinovitch, F. P. Chan, A. L. Marsden, J. A. Feinstein, Evolution of hemodynamic forces in the pulmonary tree with progressively worsening pulmonary arterial hypertension in pediatric patients, *Biomechanics and Modeling in Mechanobiology* 18 (3) (2019) 779–796.
 - [106] A. Ramachandra, A. Kahn, A. Marsden, Patient-Specific Simulations Reveal Significant Differences in Mechanical Stimuli in Venous and Arterial Coronary Grafts, *Journal of Cardiovascular Translational Research* 9 (279–290) (2016) 4.
 - [107] TaiYi System, <https://www.top500.org/system/179572/>, accessed: 2021-09-25.
 - [108] H. Kim, I. Vignon-Clementel, J. Coogan, C. Figueroa, K. Jansen, C. Taylor, Patient-specific modeling of blood flow and pressure in human coronary arteries, *Annals of Biomedical Engineering* 38 (10) (2010) 3195–3209.
 - [109] S. Sankaran, M. Esmaily Moghadam, A. M. Kahn, E. E. Tseng, J. M. Guccione, A. L. Marsden, Patient-specific multiscale modeling of blood flow for coronary artery bypass graft surgery, *Ann Biomed Eng* 40 (10) (2012) 2228–2242.
 - [110] N. Gutierrez, M. Mathew, B. McCrindle, J. Tran, A. Kahn, J. Burns, A. Marsden, Hemodynamic Variables in Aneurysms are Associated with Thrombotic Risk in Children with Kawasaki Disease, *International Journal of Cardiology* 281 (2019) 15–21.

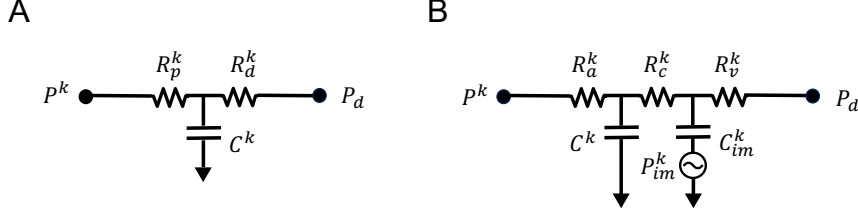


Figure A.1: Schematics of the (A) three-element Windkessel and (B) coronary outlet models commonly used in cardiovascular simulations.

Appendix A. Zero-dimensional models for Neumann coupling

Appendix A.1. Three-element Windkessel model

The three-element Windkessel model (Figure A.1A), commonly known as the RCR model and described with the differential-algebraic equations below, models the compliance of the downstream vasculature with a capacitance C^k , the resistance of the downstream arteries with a proximal resistance R_p^k , and the resistance of the downstream capillaries and veins with a distal resistance R_d^k ,

$$\frac{dP_c^k}{dt} = \frac{Q^k}{C^k} - \frac{P_c^k - P_d^k}{R_d^k C^k}, \quad P^k = P_c^k + R_p^k Q^k,$$

wherein P_c^k is the pressure proximal to the capacitance C^k , and P_d^k is the distal reference pressure.

Appendix A.2. Coronary model

The coronary model (Figure A.1B) similarly models the compliance of the downstream vasculature with a capacitance C^k and the resistance of the downstream arteries, capillaries, and veins with corresponding resistances R_a^k , R_c^k , and R_v^k , respectively,

$$\frac{dP_c^k}{dt} = \frac{Q^k}{C^k} - \frac{P_c^k - P_{c,im}^k}{R_c^k C^k}, \quad \frac{dP_{c,im}^k}{dt} = \frac{P_c^k - P_{c,im}^k}{R_c^k C_{im}^k} - \frac{P_{c,im}^k - P_d^k}{R_v^k C_{im}^k} + \frac{dP_{im}^k}{dt}, \quad P^k = P_c^k + R_a^k Q^k.$$

The addition of an intramyocardial capacitance C_{im}^k (with a corresponding proximal pressure $P_{c,im}^k$) and intramyocardial pressure P_{im}^k , however, are distinctive features that capture the out-of-phase behavior of coronary flow relative to aortic flow. Namely, the increased resistance due to ventricular contraction yields restricted coronary flow during systole. Depending on the location of the coronary artery of interest, P_{im}^k is prescribed as either the left or right ventricular pressure over time. Readers may refer to [108, 109, 110] for more details.